

**Futuristic Kusachiite Solar Cells of  $\text{CuBi}_2\text{O}_4$   
Absorber and Metal Sulfide Buffer Layers:  
Theoretical Efficiency Approaching 28 %**

**M.Tech. Thesis**

By

**D. Yashwanth Kumar Reddy  
(2002105006)**



**DISCIPLINE OF METALLURGY AND MATERIALS SCIENCE  
INDIAN INSTITUTE OF TECHNOLOGY INDORE**

**May 2022**

**Futuristic Kusachiite Solar Cells of  $\text{CuBi}_2\text{O}_4$  Absorber and Metal Sulfide Buffer Layers: Theoretical Efficiency Approaching 28 %**

**A THESIS**

*Submitted in partial fulfillment of the requirements for the award of the degree of*  
**Master of Technology**

*by*

**D. YASHWANTH KUMAR REDDY**



**DISCIPLINE OF METALLURGY AND MATERIALS SCIENCE  
INDIAN INSTITUTE OF TECHNOLOGY INDORE**

**May, 2022**



# INDIAN INSTITUTE OF TECHNOLOGY INDORE

## CANDIDATE'S DECLARATION

I hereby certify that the work which is being presented in the thesis entitled **Futuristic Kusachiite Solar Cells of  $\text{CuBi}_2\text{O}_4$  Absorber and Metal Sulfide Buffer Layers: Theoretical Efficiency Approaching 28 %** in the partial fulfillment of the requirements for the award of the degree of **MASTER OF TECHNOLOGY** and submitted in the **DISCIPLINE OF METALLURGY AND MATERIALS SCIENCE, Indian Institute of Technology Indore**, is an authentic record of my own work carried out during the time period from August 2020 to May 2022 under the supervision of Dr. Rupesh S. Devan, Associate Professor, Indian Institute of Technology Indore, and Parasharam M. Shirage, Associate Professor, Indian Institute of Technology Indore.

The matter presented in this thesis has not been submitted by me for the award of any other degree of this or any other institute.

(D. Yashwanth Kumar Reddy)

-----  
This is to certify that the above statement made by the candidate is correct to the best of my/our knowledge.

Dr. RUPESH S. DEVAN

Prof. PARASHARAM M. SHIRAGE

-----  
D. Yashwanth Kumar Reddy has successfully given his M.Tech. Oral Examination held on 03/06/2022.

Signature(s) of Supervisor(s) of M.Tech. thesis  
Date: 03/06/2022

14.06.2022  
Dr. A.K. Kushwaha  
Act. Convener, DPGC  
Date:

Signature of PSPC Member #1  
Date: 08.06.2022

Signature of PSPC Member #2  
Date: 08/06/2022

-----



## **ACKNOWLEDGEMENTS**

I take this opportunity to express my deep sense of respect and gratitude for Dr. Rupesh S. Devan for believing in me to carry out this work under his supervision. His constant encouragement, friendly interactions, and constructive support have enabled this work to achieve its present form. His innovative perspective toward things and his continuous pursuit of perfection have profoundly affected me and transformed me significantly. I feel incredibly privileged to be one of his students. His encouragement led me to learn many things. He supported me all the way and helped me learn a multi-faceted approach. I am thankful to my other supervisor Prof. P. M. Shirage, for his constant encouragement and help in this work. I am thankful to IIT Indore for allowing me to carry out the research work and providing all the facilities. I am enormously grateful to Mr. Vishesh Manjunath and Mr. Santosh Bimli for guiding and helping me out from the first day I joined this project. I would also like to thank Ms. Sameena Rapphik Mulani and Mr. Diwakar Singh for their constant support. I want to express gratitude to other members of the Nano-architectures research group for their moral support and the friendly nature we have created in our lab. Lastly, but undoubtedly the most valued, gratitude is expressed to my parents for letting me choose my dreams and supporting me endlessly. Your unmatched support made this work possible.

## Abstract

Solar cells exhibit high performance using a thin semiconducting film with superior light-harvesting ability. Though a variety of thin-film solar cells have shown promise, they suffer from long-term stability, strenuous processing, and high cost. This study evidence the capabilities of cheap and stable copper bismuth oxide or  $\text{CuBi}_2\text{O}_4$  (CBO) as an efficient light absorber for thin-film photovoltaics. Solar Cell Capacitance Simulator-1D (SCAPS-1D) software is used to optimize the performance of CBO-based kusachiite solar cells with various n-type metal sulfide (MS) buffer layers ( $\text{CdS}$ ,  $\text{WS}_2$ ,  $\text{SnS}_2$ , and  $\text{ZnS}$ ). The variation in the thickness of CBO light absorber and MSs buffer layers film had the highest control over power conversion efficiency (PCE) and other solar cell parameters. The effect of the work function of metal back contact and operating temperature on the performance of solar cells is also analyzed to assess the real-time application of the proposed metal sulfide and CBO-based kusachiite solar cells. The highest efficiency of 27.73 % is observed for ITO/ $\text{SnS}_2$ /CBO/Au solar cell device structure; however, the optimized solar cell device structure of ITO/ $\text{WS}_2$ /CBO/Au showed a theoretical PCE of 22.84% in terms of thickness and doping density. CBO is synthesized by the hydrothermal route and characterized for phase purity, morphology, bandgap, and elemental composition through XRD, FESEM, UV-Vis, and XPS techniques.

## LIST OF PUBLICATIONS

1. **Yashwanth K. Reddy**<sup>1</sup>, Vishesh Manjunath<sup>1</sup>, Santosh Bimli, and Rupesh S. Devan “Futuristic Kusachiite Solar Cells of CuBi<sub>2</sub>O<sub>4</sub> Absorber and Metal Sulfide Buffer Layers: Theoretical Efficiency Approaching 28 %” (Manuscript Submitted). (1: authors sharing equal contribution)
2. Vishesh Manjunath<sup>1</sup>, **Yashwanth K Reddy**<sup>1</sup>, Santosh Bimli, Ram Janay Choudhary, Rupesh S. Devan “22% efficient Kusachiite solar cells of CuBi<sub>2</sub>O<sub>4</sub> light harvester and ABO<sub>3</sub> buffer layers: A theoretical analysis” (Manuscript Submitted). (1: authors sharing equal contribution)
3. Santosh Bimli<sup>1</sup>, **Yashwanth K Reddy**<sup>1</sup>, Vishesh Manjunath, Rupesh S Devan “All oxide solar cells of kusachiite CuBi<sub>2</sub>O<sub>4</sub> light harvester and metal oxide buffer layers: a theoretical study” (Manuscript Submitted). (1: authors sharing equal contribution)

# TABLE OF CONTENTS

<b>LIST OF FIGURES</b>	<b>vi</b>
<b>LIST OF TABLES</b>	<b>viii</b>
<b>NOMENCLATURE</b>	<b>ix</b>
<b>Chapter 1: Introduction</b>	
<b>1.1 Energy framework till date</b>	<b>1</b>
<b>1.2 Different generations of Solar cells</b>	<b>2</b>
1.2.1 First Generation Solar cells	3
1.2.2 Second Generation Solar cells	3
1.2.3 Third Generation Solar cells	4
1.2.4 Tandem Solar cells	4
1.2.5 Challenges	4
<b>1.3 Components of Solar cell</b>	<b>5</b>
1.3.1 Transparent Conductive Oxide	5
1.3.2 Electron Transport Layer	5
1.3.3 Absorber Layer	5
1.3.4 Hole Transport Layer	6
<b>1.4 Solar Cell Parameters</b>	<b>6</b>
1.4.1 Open Circuit Voltage ( $V_{oc}$ )	7
1.4.2 Short Circuit Current ( $J_{sc}$ )	7
1.4.3 Fill Factor (FF)	7
1.4.4 Efficiency ( $\eta$ )	8
1.4.5 Series Resistance	8
1.4.6 Shunt Resistance	8
1.4.7 Recombination Losses	8
1.4.8 Optical Losses	9
<b>1.5 Working Principle and Device Architecture</b>	<b>9</b>
<b>1.6 Literature Review and Problem Formulation</b>	<b>10</b>

<b>Chapter 2: Experimental Section</b>	<b>15</b>
<b>2.1 Hydrothermal Method</b>	<b>15</b>
<b>2.2 SCAPS-1D Simulation</b>	<b>16</b>
<b>2.3 Characterization Techniques</b>	<b>19</b>
2.3.1 FESEM & EDS	19
2.3.2 XRD Spectroscopy	20
2.3.3 UV-Vis Spectroscopy	21
2.3.4 XPS	22
<b>Chapter 3: Results and Discussion</b>	<b>25</b>
<b>3.1 Simulation Results</b>	<b>25</b>
3.1.1 Absorbance	25
3.1.2 Absorber Thickness Layer Optimization	26
3.1.3 Absorber Layer Doping Variation	27
3.1.4 Absorber Defect density	28
3.1.5 Donor thickness Optimization	29
3.1.6 Donor density Optimization	29
3.1.7 Work Function Optimization	30
3.1.8 IPCE Variation	32
3.1.9 Temperature Dependence	32
<b>3.2 Experimental Results</b>	<b>36</b>
3.2.1 FESEM & EDS	36
3.2.2 X-Ray Diffraction Measurements	36
3.2.3 UV-Vis Spectroscopy	37
3.2.4 X-Ray Photoelectron Spectroscopy	38
<b>Chapter 4: Conclusions and Scope for Future Work</b>	<b>41</b>
<b>REFERENCES</b>	<b>43</b>

# LIST OF FIGURES

Figure 1.1: Cumulative Installed Power Capacity in India as of 31/3/2020

Figure 1.2: Classification of Solar cells based on generations

Figure 1.3: Different architectures of perovskite solar cells

Figure 1.4: **(a)** Comparison of Shockley-Queisser efficiency limits of various light harvesters.

Figure 1.4: **(b)** Schematics of proposed CBO and metal sulfide based Kusachiite solar cells.

Figure 2.1: Energy band diagram of p-type CBO light absorber and various n-type metal sulfide buffer layers utilized for p-n junction solar cell.

Figure 2.2: Schematic of FESEM

Figure 2.3: Schematic of X-ray Diffraction apparatus

Figure 2.4: Schematic of UV-Vis Spectrophotometer

Figure 2.5: Schematic of X-ray photoelectron spectroscopy

Figure 3.1: Simulated absorption coefficient of CBO light absorber layer

Figure 3.2: The effect of CBO light absorber thickness on the performance of solar cells comprising 100 nm thick buffer layers of various sulfide films

Figure 3.3: The effect of acceptor doping density of 900 nm thick CBO light absorber film on the performance of solar cells comprising various sulfide buffer layers of 100 nm thickness

Figure 3.4: The effect of bulk defect density of 900 nm thick CBO light absorber film on the performance of solar cells comprising various sulfide buffer layers of 100 nm thickness

Figure 3.5: The effect of thickness of MSs buffer layers on the performance of solar cells comprising 900 nm thick CBO absorber layer

Figure 3.6: The effect of donor density of 100nm thick MSs buffer layers on the performance of solar cells comprising CBO absorber layer of 900 nm thickness

Figure 3.7: The effect of work-function of metal back contact on various parameters of solar cells consisting of optimized CBO and MSs thin layers

Figure 3.8: IPCE curves of the kusachiite solar cells for different CBO absorber thicknesses with optimized thickness of various **(a)** CdS, **(b)** WS<sub>2</sub>, **(c)** SnS<sub>2</sub>, and **(d)** ZnS buffer layers

Figure 3.9: J-V curves of kusachiite solar cells comprising spinel CBO absorber and n-type CdS, WS<sub>2</sub>, SnS<sub>2</sub>, and ZnS buffer layer

Figure 3.10: Temperature-dependent J-V curves of the kusachiite solar cells containing spinel CBO absorber and n-type MSs buffer layer

Figure 3.11: FESEM images of hydrothermally synthesized CuBi<sub>2</sub>O<sub>4</sub> powder

Figure 3.12: EDS spectrum of hydrothermally synthesized CuBi<sub>2</sub>O<sub>4</sub> powder

Figure 3.13: Rietveld Refined Pattern of Pure phase of CBO

Figure 3.14: UV-Vis diffuse reflectance spectroscopy of CBO nanostructure

Figure 3.15: Kubelka-Munk plot of as synthesized CBO nanostructure

Figure 3.16: XPS Plots of the powder sample

## **LIST OF TABLES**

Table 1 The physical parameters used to analyze and optimize solar cell properties.

Table 2 The defect parameters used to analyze and optimize solar cell properties.

Table 3 Rietveld Refinement Parameters of the sample

# NOMENCLATURE

$\Psi$	Electrostatic potential
$q$	Electron charge
$\epsilon$	Dielectric constant of the semiconductor material
$p$ & $n$	hole concentration & electron concentration
$N_A^-$ & $N_D^+$	Density of the ionized acceptors & the ionized donors
$n_t$ $p_t$	Trapped electrons & Trapped holes
$x$	Position coordinate.
$G_n$ & $G_p$	Electron and hole generation rates.
$n_p$ & $p_n$	Electron and hole concentrations in p-region and n-region
$n_{p0}$ & $p_{n0}$	Equilibrium electron and hole concentrations in p-region and n-region
$\tau_n$ & $\tau_p$	Electron and hole lifetime
$\mu_p$ & $\mu_n$	Hole and electron mobilities
$E$	Electric field
$D_n$ & $D_p$	Electron and hole diffusion co-efficient
$E_{Fn}$ & $E_{Fp}$	Quasi-Fermi levels for electrons and holes
SEM	Scanning Electron Microscopy
DSSC	Dye-Sensitized Solar Cells



# Chapter 1

## Introduction

### 1.1 Energy Framework till date

The energy powering the world seems unseen yet felt. A few examples of energy production are using fossil fuels like petroleum and coal. These processes use fossil fuels to generate heat and impart the same to a prime mover (Water) to generate electricity; as globalization proceeds, energy demands increase, bringing pressure on energy requirements. The depletion rate of fossil fuels is rising due to energy consumption. Researchers are investigating alternate energy sources for offsetting the world's energy balance. Renewable energy sources are bountiful sources and can be employed for electricity generation. Solar, wind, hydro, tidal, and geothermal energy belong to this category. India's current renewable energy scenario is shown in the picture below. The Indian government is keen on increasing dependence on renewables soon.

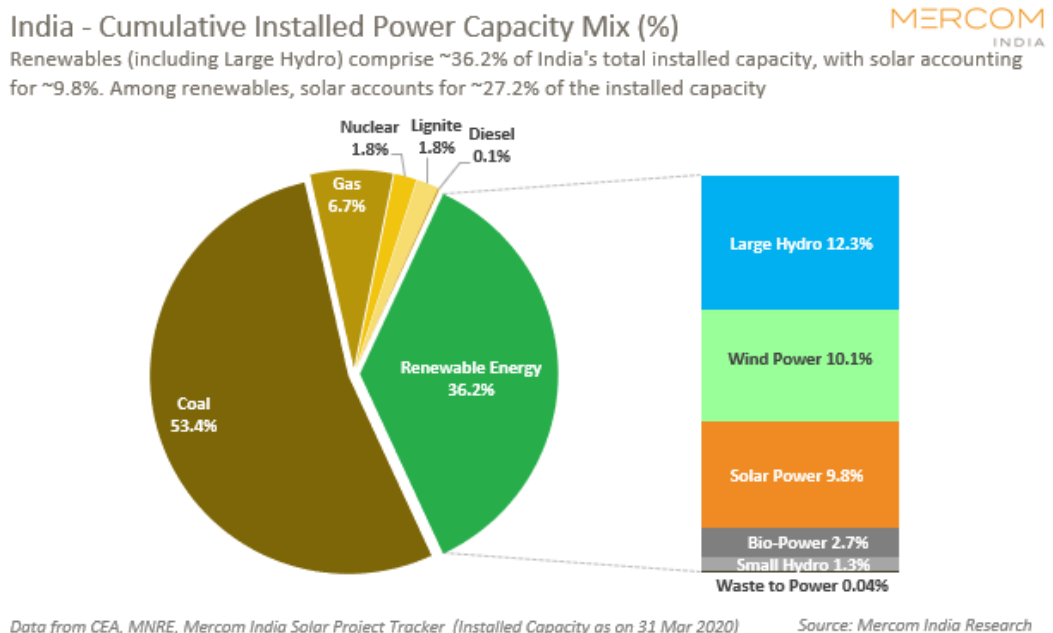


**Figure 1.1** Cumulative Installed Power Capacity in India as of 31/3/2020 [1]

The Terawatt challenge is a call for renewable energy production. It involves harvesting renewable energy sources to offset energy demands. Richard E

Smalley coined the Terawatt challenge to view renewable energy dependence increase [2]. He emphasized that harvesting renewable energy sources is the way forward for fulfilling the world's energy needs. The challenge became a big part of the green initiative and paved a direction to begin a quest to harness alternate sources of energy. Solar energy is in the limelight because of its abundance. Researchers laid basic principles for direct and indirect harvesting of solar energy. Some indirect solar energy harvesting processes include heating purposes, storing the solar energy in molten salts, Trombe walls, etc. Solar concentrators focus incident solar energy on water-carrying pipes. The concentration of light on pipelines will heat the water. This water heating method is used in the residential environment by eliminating conventional heaters or geysers. Industrial use of the same phenomenon involves heating molten salts, which hold energy much more efficiently than steam from a thermodynamic standpoint. Trombe walls are built into houses to achieve temperature management. They are walls facing maximum sun painted with black color as it absorbs solar energy best. Effective operation includes thermal insulation and air gap between glass and wall. In the process, the wall absorbs sunlight during daytime due to thermal lag introduced between outside and inside walls by high heat capacity materials heat seeping takes time. The timing of heat seeping is calibrated such that heat seeps in the nighttime, warming the room without any external heaters [3].

A solar cell is a device that transforms light incident on it into electricity based on the photovoltaic effect. The basis of the photovoltaic effect is that the incident photon will impart the necessary energy to the electron. The electron then gains the power to move about the bulk of the material. The electron, when it flows through metal contact, generates electricity.

## **1.2 Generations of Solar Cells**

Research on solar cells started approximately 45 years ago. Researchers investigated many materials, developed many methods of fabrication, and classified solar cells on the grounds of absorber materials. There are four generations named First, Second, Third, and emerging solar cells. Pictorial representation is attached below [4].

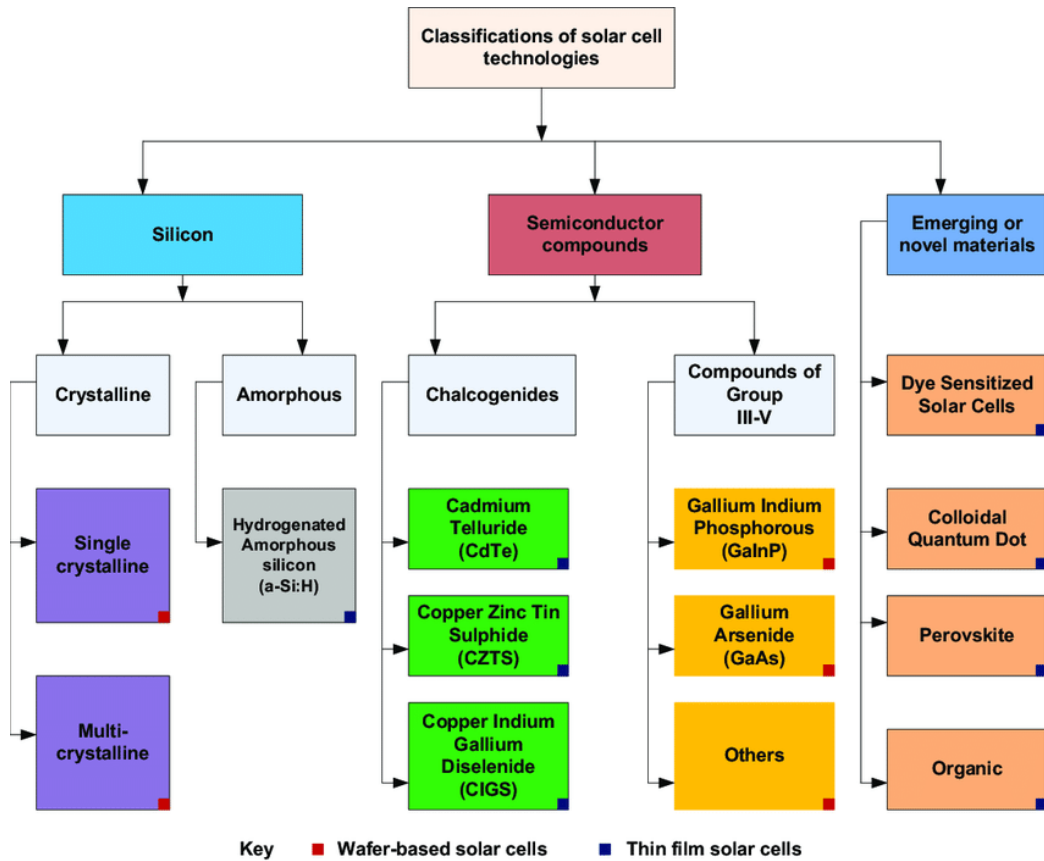


**Figure 1.2** Classification of Solar cells based on generations.

### 1.2.1 First generation solar cell

First-generation cells consist of single-crystal wafer-based solar cells. Researchers investigated the stability and performance of these cells. A large area of operation is essential for reliable results. Fabrication of single-crystal silicon involves elevated temperature and immense effort to make the most of the production cost [5]. Researchers compromised crystallinity for efficiency and employed amorphous silicon for solar cells. Disorder in structure hinders carrier movement, causing a drop in efficiency compared to single-crystal cells [6].

### 1.2.2 Second-generation solar cell

These cells are famously known as thin-film flexible solar cells. Their flexibility does not affect their functioning [7]. This nature makes them easier to employ in complex shapes for power generation. These performed better than first-generation ones at a lesser material weight and a lesser thickness. Fabrication of these cells does not require complex production methods or stricter requirements like single crystallinity. The downside of these cells is the toxicity of cadmium, a principal element/material. Even arsenic falls in this classification. Some examples

are CdTe, CIGS, GaAs, and others. The cost of these cells varies with the elements employed. Indium and arsenic increase the cost of the cell [8].

### **1.2.3 Third generation solar cell**

This generation uses organic materials as an absorber layer. Electrolytes are employed to transport the electrons to metal contacts. These types of cells are Dye-Sensitized Solar cells (DSSC). Generally, dye is the conducting medium for the cell. Polymer solar cells fall in the same category apart from these Perovskite solar cells[9]. The overall cost of the cell decreases due to organic replacements. Hybrid organic-inorganic perovskites achieved high efficiency; however, instability has a low market value. Research into fabrication methods of these cells revealed simple processes. Spin coating, drop-casting, and doctor blading are a few methods to name, and these are scalable [10].

### **1.2.4 Tandem solar cell**

A Tandem indicates more than one junction in a single cell. This concept uses a bandgap of separate junctions to increase absorption efficiency. Exploration into combinations of the same is in PV Community. Bandgap plays a vital role in selecting the absorber materials. Researchers are experimenting with combining first-generation and second-generation solar cells on a bandgap basis to absorb the said spectrum completely. Research on choosing a suitable bandgap for complete solar spectrum absorption is rising [11].

### **1.2.5 Challenges**

Although solar cells show promising results, a few limitations cropped up, ranging from practicality, fabrication, and toxicity to name a few. Some of these limitations apply to each generation, mostly one at a time. Fabrication methods for synthesizing first-generation solar cells are costly. Though second-generation solar cells offer less complex fabrication methods, they come with toxicity due to their material choice. Take the example of cadmium in CdTe solar cell, which is high on a toxic ladder, particularly for humans [12]. Indium increases the cost of solar cells in CIGS. Perovskite solar cells employ organic and inorganic absorbers, making them susceptible to degradation through ambient moisture [13]. DSSC has its fair share of concerns in terms of electrolytes working. A new type of material choice that averts the current predicament is the way researchers are investigating [14-16].

### **1.3 Components of solar cells**

Solar cells possess a transparent conducting oxide substrate, ETL, HTL, absorbing layer, and metal contacts. All generations of solar cells follow the same dogma; however, PV Community obtained new architectures by omitting either transport layer. Transport layer-free solar cells are the coined name for these cells.

#### **1.3.1 Transparent Conducting Oxide (TCO)**

TCO is a thin film grown on a glass substrate. It is optically transparent, allows light, and is electrically conductive. It acts as back contact to complete the circuit most of the time. FTO and ITO are ever-present oxide layers in solar cell fabrication. TCO should possess a more than 3.2 eV bandgap value to allow sunlight to pass through them without obstruction. Flexible substrates find their use in second-generation solar cells. Polyamide materials are tested apt for this application [17].

#### **1.3.2 Electron transport layer (ETL)**

As the name suggests, ETL allows electrons to pass through, i.e., acts as a pathway for electrons generated in the absorber layer. Electrons thus generated reach FTO through ETL, eventually an external circuit. ETL also blocks hole movement and effectively stops recombination[18]. Materials used for ETL are n-type. ETL should always be transparent to visible light for the functioning of a photovoltaic device. Pre-requisites for material to function as ETL are high mobility in comparison with that of absorber layer to avoid charge accumulation[19]. Recombination length should be more than the thickness of the layer to ensure carriers reach FTO or ITO without undergoing recombination during transport.

#### **1.3.3 Absorber Layer**

The absorber layer absorbs the incoming visible light, and the light frees electrons forming electron-hole pairs. In principle, this layer should possess a high diffusion length to allow a flexible thickness, good carrier mobility to allow carrier movement, less trap density, or defects present in the materials serving as trap states/ defect sites. An essential aspect of this layer is to show good absorption over the visible spectrum to generate carriers upon photon incidence [20, 21].  $\text{CuBi}_2\text{O}_4$  (CBO) belongs to the spinel family of structure  $\text{AB}_2\text{O}_4$ . Metals mostly occupy A and B sites. Spinel structures are divided into normal and inverse types based on

occupation sites of A and B materials in the structure's classification [22]. The theoretical crystal structure is a simple cubic structure with oxygen occupying 48e Wyckoff positions, B-site material occupying 16d Wyckoff positions, and A-site at 8c Wyckoff positions. Attributes of spinel structure are cubic close-packed structures with eight tetrahedral and four octahedral sites in the unit cell [23]. The intent of choosing this material is to maximize resistance against atmospheric degradation while retaining visible light absorption and offering a simple synthesis method.

### 1.3.4 Hole Transport Layer (HTL)

HTM transports hole-generated holes in the absorber layer to metal contact. It allows holes exclusively, extraction, and blocks electrons, thereby preventing a short circuit of the device. For absorber material, both transport layers should satisfy the bandgap alignment. HTM-free devices are possible if the absorber material is amphoteric or designed as a p-n junction device [24]. The overall cost of the device reduces in terms of materials used and cost per watt.

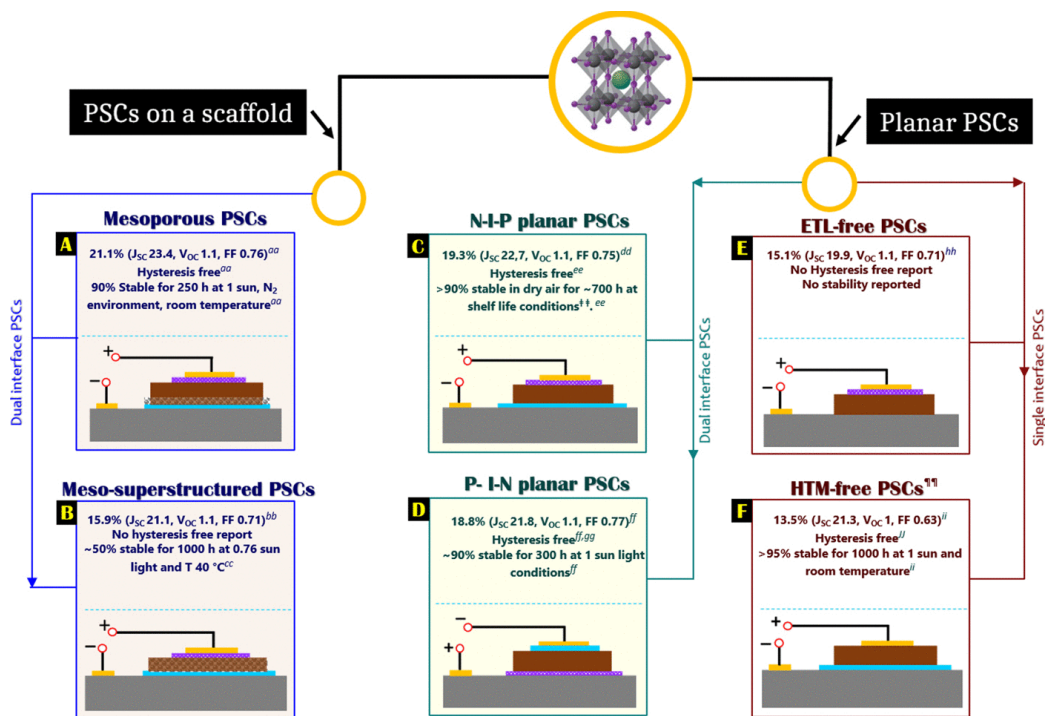


**Figure 1.3** Different architectures of perovskite solar cells [25]

### 1.4 Solar cell parameters

Solar cells are evaluated by four parameters like Open circuit voltage ( $V_{oc}$ ), Short circuit current ( $J_{sc}$ ), Fill Factor (FF), and Power Conversion Efficiency

(PCE). I-V characteristics and the above parameters determine efficiency. Solar cell simulation is done at room temperature and standard test conditions, i.e., total irradiance on the cell should be 1000 W/m<sup>2</sup>, and the spectrum resembles the traditional AM1.5G spectrum [26].

#### **1.4.1 Open Circuit Voltage (Voc)**

This voltage is the maximum amount that the circuit can maintain and occurs at zero current. It represents the quantity of forwarding bias on the p-n junction (diode) when the incident visible light generates a photocurrent. Forward bias in the solar cell occurs when voltage is applied to reduce the electric field or depletion region formed by the junction. The reduced gap leads to higher diffusion of carriers and diffusion current.

#### **1.4.2 Short Circuit Current (Jsc)**

The maximum value of current assuming trough at zero voltage is short circuit current. Absorbed photons through the material contribute to electron-hole pairs generating a photocurrent. Short circuit current may be the most considerable amount collected from the solar cell. Jsc differs by the following parameters: light-exposed area, light intensity, absorption coefficient, and collection probability. The light intensity translates to the quantity of photons incident on the surface per unit. The absorption coefficient is the parameter determining the photon translation rate into the electron-hole pair. Collection probability is when the generated carrier will be collected by the p-n junction and contributes to the photocurrent. Diffusion length and cell thickness play an essential role in deciding collection probability. Diffusion length limits the distance of carrier movement, and a cell thickness beyond diffusion length invariably leads to undesirable recombination. Jsc is area dependent. current density (Jsc) is used per unit area to eliminate area dependence

#### **1.4.3 Fill Factor (FF)**

FF is the next essential element in the characterization of the solar cell. It is the ratio of maximum power generated to the product of Voc and Jsc. The power generated is zero at points of Voc and Jsc. Power extraction should happen at an optimum point from an efficiency point of view. It represents the squareness of the I-V curve. The fill factor shows nearness to the ideal solar cell.

#### **1.4.4 Efficiency**

All power generation devices are characterized by efficiency. It is the ratio of power generated by the cell to the power available in the form of incident light. It is a measure of light converted into electricity by the cell. Efficiency depends on parameters like  $V_{oc}$ ,  $J_{sc}$ , and FF. These parameters are dependent on the fabrication process, and efficiency is, in turn, dependent on them.

#### **1.4.5 Series Resistance ( $R_s$ )**

Series resistance is a parasitic resistance caused by contact of the metal electrodes towards movement inside the cell. As series resistance increases, the drop in voltage also increases and causes a decrease in the efficiency. Series resistance and fill factor are in inverse relations; an increase in series resistance moves cell behavior away from solar cells.

#### **1.4.6 Shunt Resistance ( $R_{sh}$ )**

Shunt resistance is due to the improper design of solar cells. It refers to the short-circuiting of the cell. Due to faulty design, electrons have another to move around and complete the circuit. This results in a loss of efficiency of the cell. This happens when pinholes or defects are present on the layers making up the solar cell. These pinholes provide a shortcut for the electrons to move about instead of the power generating. This will reduce the total current flowing in the circuit.

#### **1.4.7 Recombination Losses**

Recombination is the phenomenon where an excited electron falls back into its original place and emits the absorbed energy. Recombination decreases the number of free carriers present, thereby reducing photocurrent, i.e., short circuit current. The type of recombination is specific to the material. They have been classified into three types Radiative, Non-Radiative, and Auger recombination. Radiative recombination is predominant in direct bandgap semiconductors. The electron from the conduction band recombines with a hole in the valence band, and the excess energy is released in the form of a photon. Next is the Shockley-Read-Hall recombination, which happens when defects are present in the material. Excited electrons stuck in the forbidden region fall into defects present in the same region. This type of recombination is a twofold process where electrons fall back into the trap state and then into the valence band. Effective recombination defect

level must be at the center of the forbidden energy gap. The next type of recombination is Auger recombination, which is a three-step process. Electron and hole recombine, releasing the energy in the form of heat or photons are taken up by the third carrier, another electron in the conduction band. The third electron falls back after losing energy thermally. This recombination becomes important at high carrier concentrations caused by either degeneracy of carriers or high photon incidence when a solar cell is placed under a concentrator [27].

#### **1.4.8 Optical losses**

These losses occur when light is not absorbed by the cell. Solar cells may reflect some of the light incident on them from the top and rear surface of the cell. Texturing or Anti-reflective coatings reduce the light reflected by the material. Anti-reflective coatings are made based on the refractive index. Light passes through the coating present on the solar cell, and as per the coating present, it can either undergo constructive or destructive interference [28]. The type of coating can preset the type of interference. Texturing induces a pattern on the surface of thin film to absorb more amount of light and reflect less. Photon optical path is also a crucial factor in photocurrent [29]. Photon optical path is the distance traveled until the photon loses its energy. The photon cannot effectively excite the carriers if a solar cell thickness is insufficient with the incident photon optical path [30].

#### **1.5 Working Principle**

When a visible light incident on the solar cell, the photons enter through either hole transport layers or FTO depending on cell architecture. As FTO is transparent to visible light, it will allow light to pass through. Light is absorbed into the absorber layer, and excitons are generated. These electron-hole pairs are only generated when photons possess enough energy to impart to electrons. The extent of photon energy is determined by the bandgap of absorber material. Once energy is imparted to electrons, they gain the energy to move freely around the bulk of the metal. Electrons that gain energy from photons leave empty space in their place. This is called a hole or vacant space. This is a meta-stable state and only exists for a small amount of time. Ideally, electrons and holes should cross the interface and move into respective transport layers during this period. The electrons move through the transport layer, FTO, and contribute to electricity in the external circuit[31]. Post electricity contribution electrons recombine with holes establishing

continuity. Each layer contributes to the functioning of the cell, so making the layers defect-free and uniform films is of paramount importance. Accessories like anti-reflective coatings, concentrators, and others are provided to enhance device efficiency by minimizing the losses in the cell. Anti-Reflective coating is applied to the cell as it helps to minimize the incident light getting reflected off the front and rear device and traps the light inside the solar cell [32]. Solar concentrators are devices used to concentrate the incident light onto solar cells, which has a probability of increased efficiency [33].

## **1.6 Literature Review and Problem Formulation**

The efficient utilization of solar energy to produce electricity has been the subject of intensive research because of the rapid increase in global energy demands and the need to reduce the emission of greenhouse gases from electricity generation by fossil fuels. [34] Solar energy conversion to electricity is an utterly clean energy source that can fulfill global energy demands with minimal detrimental impact on the environment. [35] Therefore, tremendous efforts have been made to develop cost-effective high PCE solar cells. Though the implementation of environmentally benign first-generation crystalline Si solar cells, with excellent charge transport properties and stability, is worthwhile with recently reduced cost, long pay pack time with modest PCE is demanding to look for a better alternative. The second-generation thin-film solar cells, i.e., CIGS, CZTS, CdTe, etc., [36] fabricated over flexible or rigid transparent substrates are found to be prolific alternatives to deliver promising efficiencies. Their ease of packaging, high power to weight ratio, flexibility, and roll to roll processing [37, 38] lead to implementation in building-integrated photovoltaics, portable power sources, powering of drones, etc.[39] However, to achieve desired photovoltaic properties, the synthesis of thin-film absorbers in required phases without other secondary phases is a skilled task. However, the PCE of single-junction thin-film solar cells is a mere ~23 % despite endless efforts from various research groups for the last three decades. [36] Moreover, third-generation solar cells such as dye-sensitized solar cells, [40] organic-inorganic halide perovskite solar cells, [41] polymer solar cells, etc., deliver the significantly higher efficiency and lower cost [42] mimicking the natural photosynthesis process have posed a challenge to replace first-generation Si solar cells.[43] Nevertheless, these perovskite solar cells suffer from thermal, moisture,

and UV interference instability.[44, 45] Consequently, diverse processes like the use of protective coatings, [46] lower-dimensional perovskites, [47] double perovskites, [48] and molten ionic salts in synthesis, [49], etc. are employed by various research groups, but interface alteration and complex fabrication processes restricted the cost-effective efficiency and long-term stability, hence require cautious optimism. Therefore, a cheap/stable alternate light absorber layer with desired photovoltaic properties is essential to overcome the drawbacks of the halide perovskite absorber layer.

On scrutinizing panchromatic visible light absorbers, p-type CBO of  $AB_2O_4$  (Kusachiite) spinel structure with tetragonal crystal system, lately studied for its implementation in solar-driven water splitting, [50] photocatalytic dye degradation, [51], and antimicrobial applications, [52] shall be an excellent choice as an absorber layer. Furthermore, CBO, a ternary metal oxide, is non-toxic, cheap, and ambient friendly and can be synthesized using various techniques ranging from solution processing to vacuum deposition. Moreover, the solar cell utilizing CBO light absorber can achieve a higher side of Shockley-Queisser limit than that of perovskite, CIGS, CZTS, and c-Si (Figure 1.4(a)). On the other hand, owing to the valence electron shell structure of the 3d orbitals, MSs have shown promise as an n-type material or emitter or buffer layer in thin-film solar cells.[53] The synthesis of MS thin films exhibiting stable physical and chemical properties and high carrier mobility is feasible from lower temperature solution or vacuum processes (even over flexible substrates) utilizing cheaper and readily available sources (Figure 1.4(b)).[54] Unlike widely used oxide buffer layers, wide bandgap MSs do not contain oxygen vacancies and facilitate high optical stability.[55] Recently, Hosen et al.[56] simulated the capabilities of CBO as absorber layer in thin-film solar cells combined with CdS in Al/FTO/CdS/CBO/Ni device architecture and estimated 26 % PCE for optimum thickness (i.e., 2000 nm) of the CBO light absorber. However, to our best knowledge, the device architecture comprising other sulfides and metal contacts has not been explored to realize the upper PCE limit of MSs/CBO.

Therefore, this study is focused on evaluating the potential of the CBO absorber layer and exploring suitable n-type MS with CBO to form efficient p-n junction thin-film solar cells shown in Figure 1.4(b). The experimental investigation to find suitable MS for CBO is a myriad task; therefore, researchers usually employ various software packages to identify the appropriate materials and analyze the

variation in solar cell performance depending on the changes in their optoelectronic properties.[57] In general, finite difference time domain method (FDTD), SILVACO ATLAS, wxAMPS, AFORS-HET, etc., are employed to simulate solar cells. However, among these software packages, SCAPS-1D, developed at Gent University, Belgium, offers a simulation of heterojunction and multi-junction solar cell devices.[58] Therefore, the suitability of n-type MSs and CBO in thin-film solar cells is analyzed based on SCAPS-1D simulations for the device structure consisting of FTO as transparent conducting oxide, n-type MS buffer layer, CBO kusachiite light absorber, and counter electrode, as shown in Figure 1.4(b). The theoretical studies on the performance of Cadmium sulfide (CdS), Tin sulfide (SnS<sub>2</sub>), Tungsten sulfide (WS<sub>2</sub>), and Zinc sulfide (ZnS) as n-type materials in combination with CBO light absorber for kusachiite solar cells are discussed comprehensively. The simplified device structure adopted in this study (FTO/MS/CBO/counter electrode) can be implemented experimentally analogous to third-generation solar cells (perovskite solar cells). The performance of solar cell parameters for simplified device structure of FTO/MS/CBO/counter electrode is evaluated for variation in thickness, acceptor/donor defect, and doping density of subsequent thin-films, counter electrodes, and operating temperature.

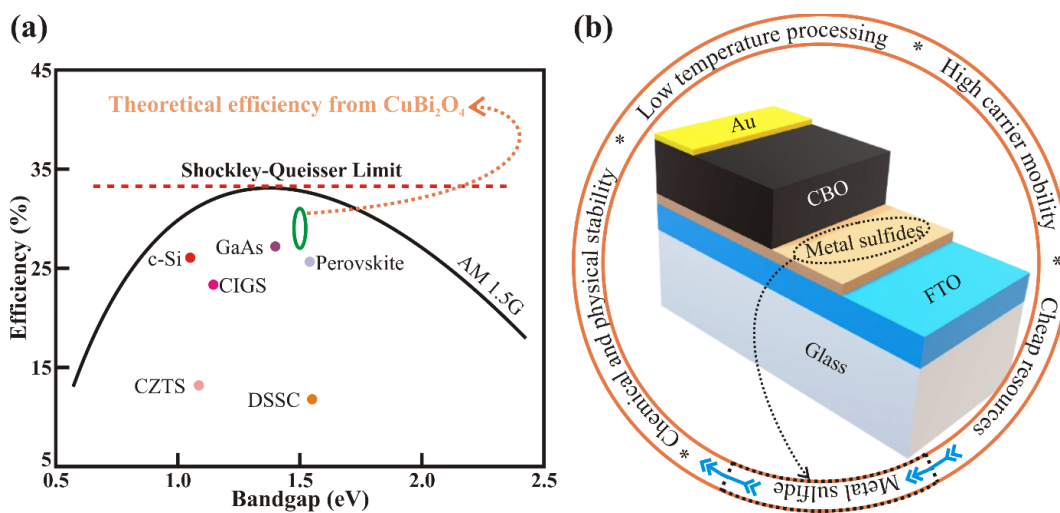


**Figure 1.4** (a) Comparison of Shockley-Queisser efficiency limits of various light harvesters. (b) Schematics of proposed CBO and metal sulfide based Kusachiite solar cells.

## Objectives

This work intends to fabricate an oxide-oxide solar cell using  $\text{CuBi}_2\text{O}_4$  as an absorber layer. A transport layer is chosen, which aligns with the band structure of the absorber. Therefore, the objective of the present work are:

1. To simulate a solar cell with CBO as the absorber.
2. To Optimize different layers of the solar cells
3. To synthesize pure  $\text{CuBi}_2\text{O}_4$  phase
4. To study morphology, phase purity, and optical properties

We have employed hydrothermal methods for the optimized synthesis of CBO. The synthesis parameters such as concentration, reaction time, and temperature are optimized. Surface morphological, crystalline, optical, and chemical properties are examined from FESEM, XRD, UV-Vis, and XPS



## Chapter 2

# Experimental Section

### 2.1 Hydrothermal Synthesis

Hydrothermal synthesis involves subjecting precursors to heat in a closed airtight container. It is a solution-based reaction method. The mode of reaction is forced hydrolysis of precursors to the final product. The formation of nanoparticles can happen in a range of room temperature to moderate temperature. The vapor pressure of the main composition in the reaction determines the morphology of synthesized nanoparticles. Nanoparticles that need higher temperatures in other routes can also be synthesized at moderate temperatures because of high pressure. As the name suggests, hydro suffix involves DI Water as a solvent to synthesize nanostructure. This reaction involves a steel container specially designed to sustain high pressures called Autoclave. It is usually made of stainless steel. The precursor solution is transferred into the autoclave. The reaction parameters like time, temperature, and concentration can be easily controlled. Hot air ovens have a built-in function to calibrate time and temperature. The concentration of precursor solutions is controlled while preparing the solution. The level of contamination and non-uniformity is high in hydrothermal methods. Physical deposition like CVD and PLD happens in a vacuum, not the case for hydrothermal synthesis. This work employs the hydrothermal method in synthesizing the material.

**Synthesis Procedure:** Firstly, 25 mM of Copper (II) Nitrate Trihydrate was dissolved in water and stirred until complete dissolution. 50 mM of Bismuth (III) Nitrate pentahydrate was entirely dissolved with the help of a magnetic stirrer in 2 M nitric acid. Both solutions were mixed and stirred for 30 minutes. The stirring was continued while 2 M NaOH solution was added to affect the reaction process. The solution changes color from transparent liquid to sky blue colored liquid. The solution was transferred to an autoclave and subjected to a hydrothermal process. The autoclave is heated to 120°C for 5 hours. The products were subjected to centrifugation and washed several times alternatively with solvents like ethanol and DI water. Then the solution was dried overnight to obtain a black-colored powder.

## 2.2 Simulation Methodology

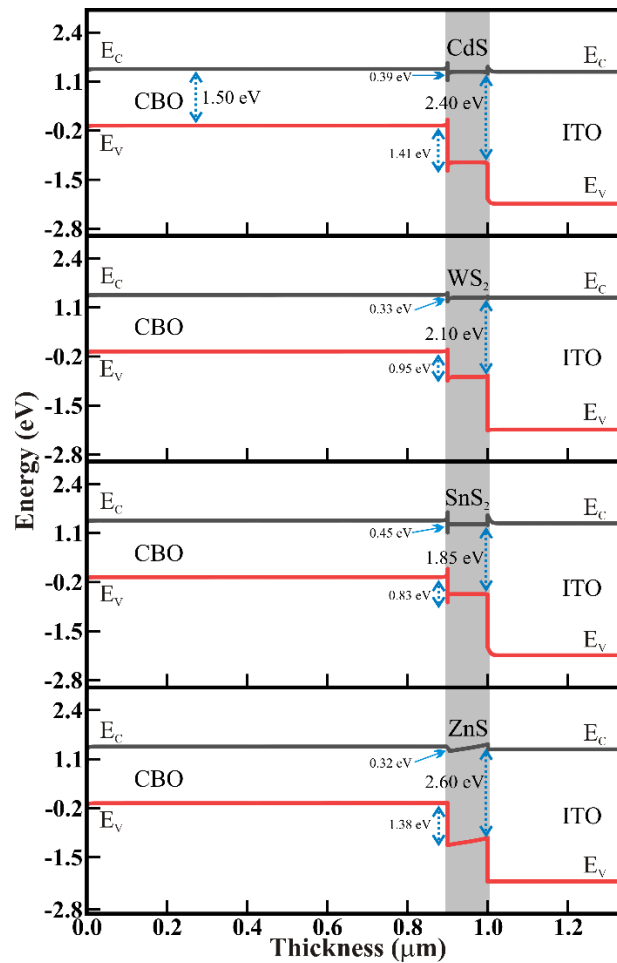


**Figure 2.1** Energy band diagram of p-type CBO light absorber and various n-type metal sulfide buffer layers utilized for p-n junction solar cell.

SCAPS-1D is a solar cell simulator developed by Marc Burgelman and his associates at the University of Gent, Belgium. It has the capacity of computing characteristics of a solar cell with a maximum of 7 layers. It was developed to simulate second-generation solar cells, but modifications were made so that it can be used for other structures as well. The effect of CBO light absorber and MSs (i.e., CdS, SnS<sub>2</sub>, WS<sub>2</sub>, and ZnS) buffer layer on the performance of kusachiite solar cells is analyzed using SCAPS-1D. The simulations are carried out under AM 1.5G with an incident power density of 100mW/cm<sup>2</sup>. The energy position of CBO with respect to the MS buffer layer is shown in [Figure 2.1](#). The conduction band offsets between CBO absorber films and CdS, WS<sub>2</sub>, SnS<sub>2</sub>, and ZnS transport layer are 0.39, 0.33, 0.45, and 0.32 eV, respectively, which offers smooth charge transportation at CBO/MS interface. [59] The barrier between the valence band maximum of CBO

and WO<sub>3</sub>, SnO<sub>2</sub>, ZnO, and TiO<sub>2</sub> buffer layer is 1.41, 0.95, 0.83, and 1.38 eV, respectively, which is sufficiently high to restrict the flow of positive carriers towards MSs, thus, minimizes recombination at the CBO/MO interface.

The solar cell performance parameters are evaluated by solving fundamental semiconductor equations mentioned below, which dictate the charge transport in the semiconductor,

Poisson Equation (Equation 1):

$$\frac{dy}{dx} = -\frac{d^2\psi}{dx^2} = \frac{q}{\epsilon} [p(x) - n(x) + N_D^+(x) - N_A^- + p_t(x) - n_t(x)] \quad (1)$$

Electron (Equation 2) and hole (Equation 3) continuity equations:

$$\frac{dn_p}{dt} = G_n - \frac{n_p - n_{p0}}{\tau_n} + n_p \mu_n \frac{dE}{dx} + \mu_n E \frac{dn_p}{dx} + D_n \frac{d^2 n_p}{dx^2} \quad (2)$$

$$\frac{dp_n}{dt} = G_p - \frac{p_n - p_{n0}}{\tau_p} + p_n \mu_p \frac{dE}{dx} + \mu_p E \frac{dp_n}{dx} + D_p \frac{d^2 p_n}{dx^2} \quad (3)$$

The carrier transport occurring by drift and diffusion for electrons (Equation 4) and holes (Equation 5) is expressed as:

$$J_n(x) = qn\mu_n E + qD_n \frac{dn}{dx} = n\mu_n \frac{dE_{Fn}}{dx} \quad (4)$$

$$J_p(x) = qp\mu_p E - qD_p \frac{dp}{dx} = p\mu_p \frac{dE_{Fp}}{dx} \quad (5)$$

The physical and defect parameters used in the simulation of PSCs are tabulated in Tables 1 and 2.

**Table 1:** The physical parameters used to analyze and optimize solar cell properties.

Parameter	ITO	CdS	ZnS	SnS <sub>2</sub>	WS <sub>2</sub>	CBO
Thickness (nm)	350			Variable		
Bandgap E <sub>g</sub> (eV)	3.5	2.4	2.6	1.85	2.1	1.5
Electron affinity $\chi$ (eV)	4	4.18	3.74	4.26	3.95	3.72
Dielectric constant $\epsilon$	9	10	12	17.7	13.6	34
CB effective density of states N <sub>c</sub> (cm <sup>-3</sup> )	2.2×10 <sup>18</sup>	2.2×10 <sup>18</sup>	2.2×10 <sup>18</sup>	7.32×10 <sup>18</sup>	2×10 <sup>18</sup>	1.2×10 <sup>19</sup>

VB effective density of states $N_v$ ( $\text{cm}^{-3}$ )	$1.8 \times 10^{18}$	$1.9 \times 10^{19}$	$1.8 \times 10^{19}$	$1 \times 10^{19}$	$2 \times 10^{18}$	$5 \times 10^{19}$
Thermal velocity of electrons $V_{\text{th,e}}$ ( $\text{cm s}^{-1}$ )	$1 \times 10^7$	$1 \times 10^7$	$1 \times 10^7$	$1 \times 10^7$	$1 \times 10^7$	$1 \times 10^7$
Thermal velocity of holes $V_{\text{th,p}}$ ( $\text{cm s}^{-1}$ )	$1 \times 10^7$	$1 \times 10^7$	$1 \times 10^7$	$1 \times 10^7$	$1 \times 10^7$	$1 \times 10^7$
Electron Mobility $\mu_n$ ( $\text{cm}^2 \text{V}^{-1} \text{s}^{-1}$ )	20	100	200	50	100	$1.1 \times 10^{-3}$
Electron mobility $\mu_p$ ( $\text{cm}^2 \text{V}^{-1} \text{s}^{-1}$ )	10	25	40	25	25	$1.2 \times 10^{-3}$
Ref.	[60]	[61, 62]	[63]	[64, 65]	[66, 67]	[56]

**Table 2** The defect parameters used to analyze and optimize solar cell properties.

Parameters	CdS	ZnS	SnS <sub>2</sub>	WS <sub>2</sub>	CBO
Defect Type	Single Acceptor	Single Acceptor	Single Acceptor	Single Acceptor	Single Donor
Capture cross section of electrons ( $\text{cm}^2$ )	$1 \times 10^{-15}$				
Capture cross section of holes ( $\text{cm}^2$ )	$1 \times 10^{-15}$				
Reference for defect energy level $E_t$	Above $E_v$				
Energy level with respect to Reference (eV)	0.6	0.6	0.6	0.6	0.6
Defect Energy Distribution	Gaussian	Gaussian	Gaussian	Gaussian	Gaussian

Characteristic Energy (eV)	0.1	0.1	0.1	0.1	0.1
Total defect density (cm <sup>-3</sup> )	1×10 <sup>14</sup>	1×10 <sup>14</sup>	1×10 <sup>14</sup>	1×10 <sup>14</sup>	variable

## 2.3 Characterization Techniques

### 2.3.1 Scanning Electron Microscopy and Energy Dispersive Spectroscopy

SEM is one of the most common characterization techniques used to determine morphology when the material is synthesized. Components in SEM are an electron gun, sample chamber, lenses, scanning coil, and detector. Carbon tape is attached to the holder to act as a ground mechanism. Electrons are emitted from the electron gun by either thermionic process or field emission. The filament is heated at a high temperature to emit electrons called thermionic emissions. The filament is heated to elevated temperatures in field emission, and the electric field is applied to the filament. Electrons are pulled from the filament due to the electric field. This is called thermionic emission. In this method, the temperature at which filament is heated can be reduced because the electrons are subjected to both heating effect and electric pull. The material used for cathode should sustain heat and have a high melting point. Electrons are accelerated by the anode. Condensing of the electron cloud is achieved by using a condenser lens. The objective lens focuses the beam to a fine point enabling a raster scan. The scan coils that produce a magnetic field deflect the beam horizontally or vertically to raster scan a rectangular sample surface area.

Electrons condensed and focused impinge on the specimen in a teardrop shape. Upon impinging the specimen, the incoming electron transfers its energy to electrons in the specimen inelastically. This energy is enough to eject electrons from the specimen surface, called back scattered electrons. These electrons are detected by the detector to generate the morphology of the specimen. SEM gives not only a top view but also a cross-sectional view of the specimen. These images are also helpful in estimating structure dimensions, e.g., the diameter of rods from the top-view and length of the rods from the cross-section view in the specimen.

**EDS** or Energy Dispersive Spectroscopy is a technique used in conjunction with FESEM apparatus to measure elemental composition present in the sample. When electrons from the emitter hit the sample, if they are energized to a high level capable of displacing core electrons of the sample, the ejected core electron is picked up by the detector. It records the intensity of each element separately and can be expressed as a percentage of total elements. The beam of electrons is focused on a particular area of the sample, and the apparatus will detect the composition of the sample.

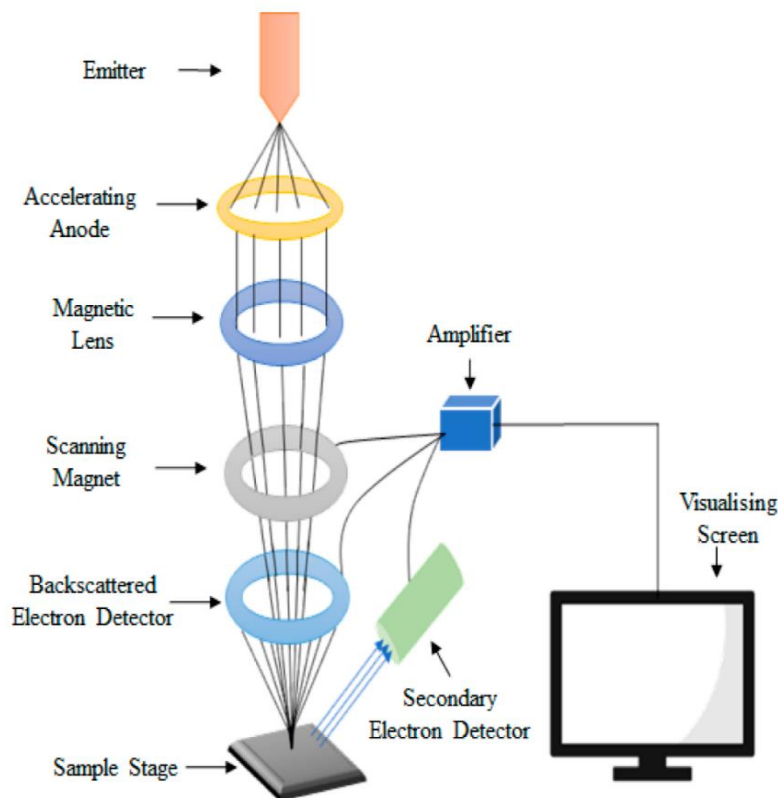


**Figure 2.2** Schematic of SEM [68]

### 2.3.2 XRD Measurements

X-Ray Diffraction (XRD) is used to study the phase crystallinity and crystallite size. The apparatus is called a diffractometer. X-Rays are produced by impinging an electron beam on target copper material. Inelastic collisions between copper material and Copper atom give rise to X-rays. These X-rays are filtered and focused on the specimen at specifically chosen angle. Target materials can be Cr, Fe, Co, Cu, and Mo but Cu is usually the option because the wavelength of X-rays produced ( $\sim 1.54 \text{ \AA}$ ) is like unit cell dimensions. Bragg's Law is the working

principle behind XRD. If the path difference of the reflected waves between two consecutive crystal lattice points is equal to the integral multiple of the incident wavelength, then constructive interference will occur between the reflected beams, and the intensity of the peaks for that plane will increase. Mathematically, Bragg's law is defined as

$$n\lambda = 2d \sin \theta$$

Where  $\theta$  is the incident angle at which the X-ray impinges the specimen, is the wavelength of the incident X-ray,  $n$  is the whole number indicating the order of diffraction peak, and  $d$  is the crystal lattice spacing. Here, Cu K(alpha) is used as an incoming X-ray. The angle is varied between  $15^\circ$  to  $80^\circ$  with a scanning rate of  $0.5^\circ/\text{min}$ . The reflections are plotted on a graph with  $2\theta$  versus the intensity of reflections. The graph is matched with the database to determine the purity of the sample. Lattice parameters were extracted from the graph with the help of FullProf software. The Rietveld method uses the least-squares method to compare the graphs of simulated patterns based on input data from the literature and graphs of experimental data.

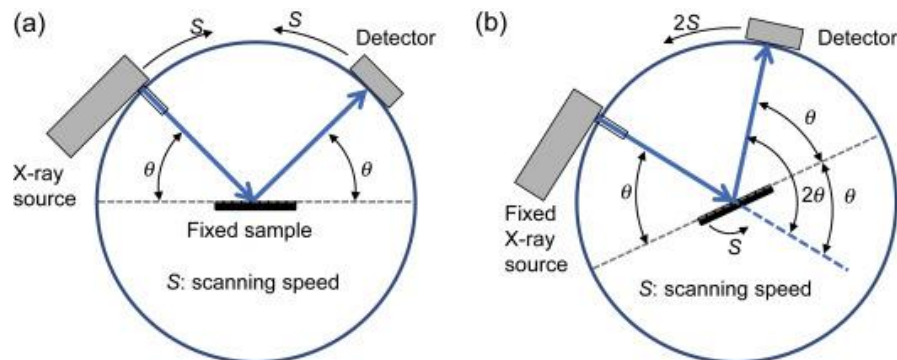


**Figure 2.3** Schematic of X-ray Diffraction apparatus [69]

### 2.3.3 UV-Vis Spectroscopy

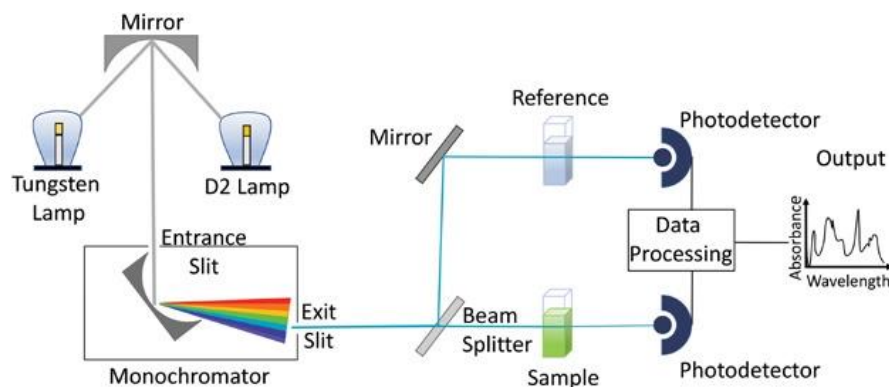


**Figure 2.4** Schematic of UV-Vis Spectrophotometer [70]

Visible light is part of the electromagnetic spectrum, which is the cause of phenomena like reflection, refraction, transmission, and absorption. Keeping aside the wave nature of light, the particle nature of light shows that light is made of photons with specific energy ( $h\nu$ ). Photons interact with matter by imparting the energy it contains to the atom/molecule photon is interacting with. The material will absorb the photons whose energy corresponds to the bandgap of the material or is greater than the bandgap of the material.

When light is irradiated on the material, some of its part is absorbed or reflected, and remaining is transmitted. The amount of light absorbed by the material is the difference between incident radiation and transmitted radiation. Quantitatively, absorbance can be defined as the logarithmic ratio of transmitted intensity to incident intensity. When optically active molecules are subjected to visible light, the electrons present take in the energy and move up the energy levels called electronic transitions. The electrons cannot maintain the position longer and fall back to the original state. The difference between the states is proportional to the energy emitted, attributed to the energy gap. The energy required by the molecules depends on their band structure and can be used to estimate the band gap. Shorter bandgaps typically correspond to the absorption of shorter wavelengths of light.

Tauc's plot is used to determine the sample's bandgap using the results of UV-Vis spectrophotometer absorbance spectra. The Kubelka Munk equation is utilized in another method called Diffuse Reflectance Method to estimate bandgap. Inhomogeneity, internal scattering variables in the sample, refractive index of the sample, and mismatch of the refractive index of the sample and immediate medium, to mention a few, are all grouped together as a semi-empirical term called Scattering Co-efficient. According to theory, the scattering co-efficient should fluctuate slowly with wavelength and considerably as packing density changes.[71, 72]

#### **2.3.4 X-ray Photoelectron Spectroscopy**

XPS realizes the photoelectric effect with the help of x-rays, thereby giving out more information about the sample. As X-rays possess high energy, they can kick off electrons from core shells and impart some kinetic energy to the core electrons. The energy of core electrons and their kinetic energy are bound by the equation,

$$E_{\text{binding}} = E_{\text{photon}} - (E_{\text{kinetic}} + \phi)$$

Where  $E_{\text{binding}}$  is the binding energy of the core electron,  $E_{\text{photon}}$  is the energy of X-ray,  $E_{\text{kinetic}}$  is kinetic energy imparted to the electron after it is kicked out from the orbit and  $\phi$  is the like work function for the specific surface of the material. The binding energy of the electron is unknown, whereas the energy of the photon or X-ray is known, the instrument measures kinetic energy, and the work function is a correction factor that involves factoring minimum energy needed to kick out an electron from the atom. The binding energy of the electron is measured by the equation above, and the oxidation state of the element is also mapped out. Subsequently, the composition of the material is also worked out. A major drawback of the XPS is that the working principle allows the instrument to measure only the core electrons coming from the sample. Elements such as Hydrogen and Helium cannot be detected with this instrument. Only electrons that have escaped from the sample into the vacuum of the instrument are detected by XPS. A photoelectron must travel through the sample in order to escape from it. Inelastic collisions, recombination, sample excitation, recapture, and confinement in various excited states inside the material can diminish the number of photoelectrons escaping. As the depth of the sample increases, these effects manifest as an exponential attenuation function, making the signals obtained from analytes at the surface much stronger than those detected from analytes deeper below the specimen surface. As a result, the XPS signal is exponentially surface-weighted, which can then be used to estimate analyte depths in layered materials.

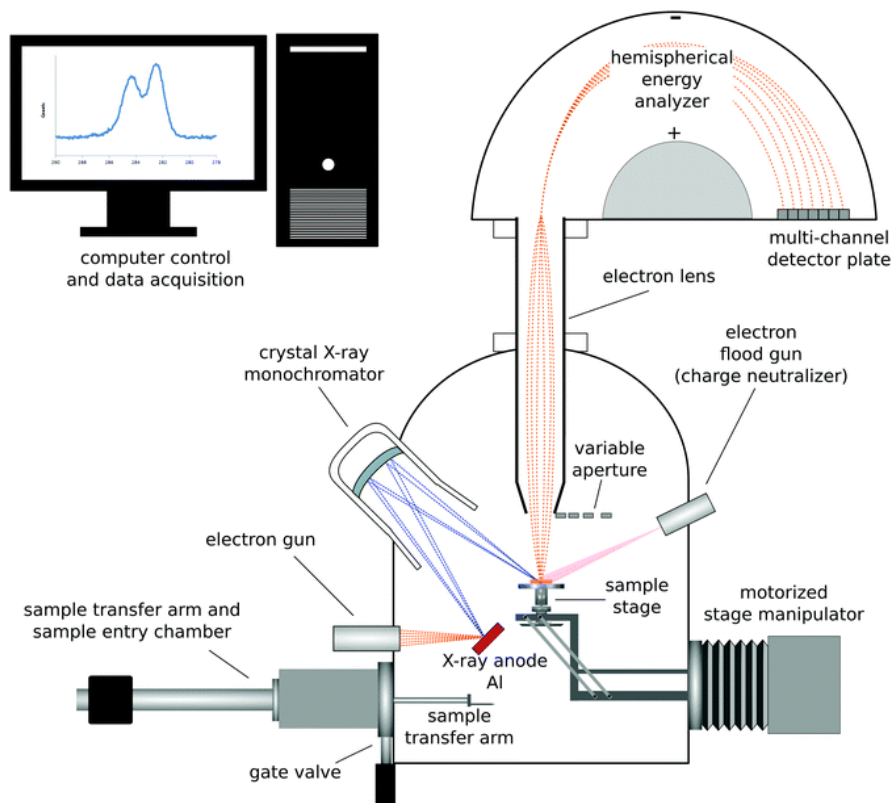


**Figure 2.5** Schematic of X-ray photoelectron spectroscopy

## Chapter 3

# Results and Discussion

### 3.1 Simulation Results

#### 3.1.1 Absorbance

The high optical absorption coefficient of the light absorbers in a thin-film format is one of the prerequisites for fabricating efficient solar cells. Therefore, the optical absorption coefficient of CBO absorbers is simulated to understand the optical absorption behavior (Figure 3.1).

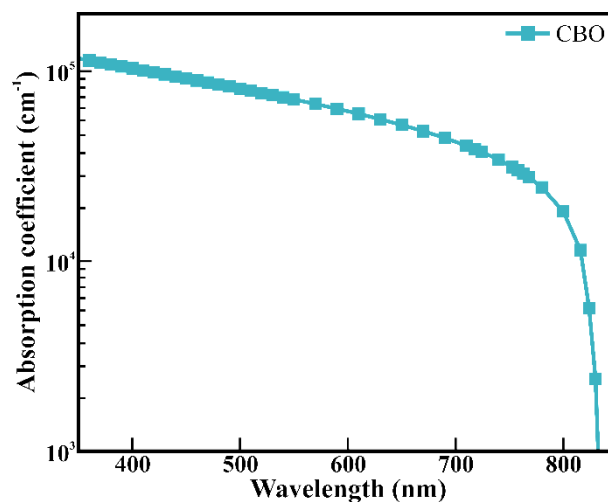


**Figure 3.1** Simulated absorption coefficient of CBO light absorber layer.

Apart from the broad absorption range in the visible spectrum, the absorption coefficient of  $\sim 10^5 \text{ cm}^{-1}$  is measured for the CBO film at 550 nm, which is relatively equivalent to high-efficiency GaAs and perovskite solar cells.[73] Another key determinant of solar cell performance is the charge-carrier diffusion length ( $L_D$ ). A longer  $L_D$  generally means a thicker absorber layer for greater light harvesting.[74] An increase in the thickness of CBO absorber film beyond the charge diffusion length will lead to charge recombination resulting in low short circuit current density ( $J_{SC}$ ), subsequently restraining the PCE.[75] Importantly, the CBO thin films deposited by spin-coating and PLD showed the carrier diffusion length of  $\sim 50 \text{ nm}$  [76, 77]. Moreover, the thickness of the absorber layer controls

the carrier absorption of short-wavelength photons and considerably reduces the electrical losses associated with charge carrier recombination at the interface. As the light absorption takes place throughout the thickness of the absorber, blue light or other high energy light is absorbed at the interface, whereas the low energy light like red light will be absorbed when the thickness of absorber is on the higher side [78]. Therefore, the thickness of CBO absorber films requires precise optimization to achieve maximum PCE.

### 3.1.2 Absorber Layer Thickness Variation

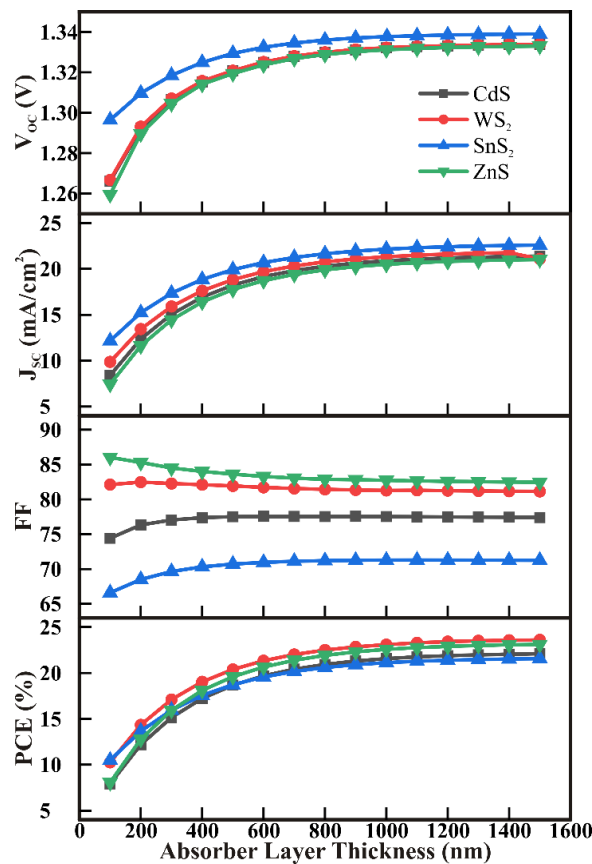


**Figure 3.2** The effect of CBO light absorber thickness on the performance of solar cells comprising 100 nm thick buffer layers of various sulfide films.

With a constant thickness of 100 nm for n-type MSs films, variation in the solar cell parameters is estimated for CBO absorber films of various thicknesses (in the range of 100 to 1500 nm), as shown in Figure 3.2. The PCE value for the solar cells consisting of n-type MSs under study (i.e., CdS, WS<sub>2</sub>, SnS<sub>2</sub>, and ZnS) increased with the thickness of CBO films due to a corresponding increase in J<sub>sc</sub>. The maximum PCE of 22.09 %, 23.6 %, 21.56 %, and 23.1 % is observed for the CdS, WS<sub>2</sub>, SnS<sub>2</sub>, and ZnS buffer layers, respectively, used with a 1500 nm thick

CBO absorber layer. However,  $J_{sc}$  and PCE are marginally saturated beyond the CBO thickness of 900 nm for all the MSs buffer layers. Although a similar trend has been observed for the fill factor (FF) and open-circuit voltage ( $V_{oc}$ ) after varying the CBO film thickness, the MS buffer layer has administered the actual gain in FF and  $V_{oc}$ . The marginal change in FF should be addressed mostly as bulk-induced changes, or losses, rather than conventional parasitic changes.[79] The marginal increment in the  $V_{oc}$  is observed with increase in absorber thickness because the band offset between CBO/MSs is independent of the thickness of the absorber layer and does not contribute to the increment in the PCE. [80-82]. The solar cells consisting of n-type  $WS_2$  showed maximum efficiency of 22.84 %, followed by ZnS (22.30 %), CdS (21.30 %), and  $SnS_2$  (20.90 %) at the CBO film thickness of 900 nm.

### 3.1.3 Absorber Layer Doping Variation

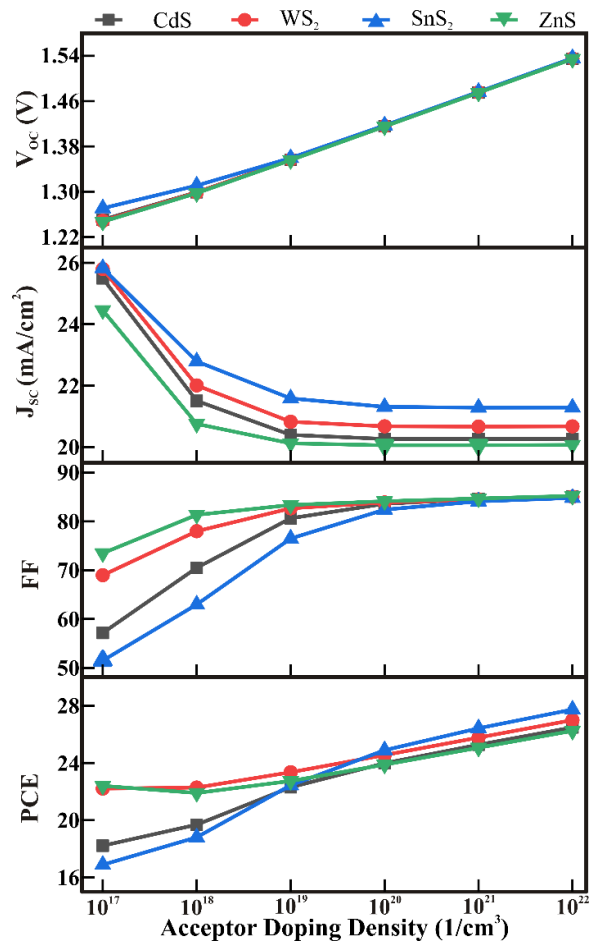


**Figure 3.3** The effect of acceptor doping density of 900 nm thick CBO light absorber film on the performance of solar cells comprising various sulfide buffer layers of 100 nm thickness.

Considering the marginal enhancement in the PCE beyond 900 nm thick CBO film, the acceptor doping density in CBO films is tuned in search of further improvement in the PCE. [Figure 3.3](#) shows the acceptor doping density-dependent variation of different solar cell parameters in the CBO films. As the acceptor doping density in the CBO film increased from  $10^{17}$  to  $10^{22}$   $\text{cm}^{-3}$ , the corresponding PCE has increased for all MSs buffer layers. The highest efficiency of 27.73 % observed for SnS<sub>2</sub> might be because of its high visible light photoactivity, followed by WS<sub>2</sub> (26.99 %), CdS (26.48 %), and ZnS (26.24 %). The  $V_{oc}$  and FF have improved with the increase in acceptor doping density, which can be ascribed to an increase in built-in potential due to modified band offset between MSs and CBO films and charge conductivity in CBO films, respectively. [83] The improved  $V_{oc}$  and FF are the significant contributors to a substantial rise in PCEs. However, the slight decrease followed by saturation in  $J_{sc}$  can be due to the higher recombination rate and a reduction in charge carrier mobility with varying acceptor doping density.[83]

#### **3.1.4 Absorber Defect density**

The solution processing or vacuum deposition techniques inculcate the bulk defect in the deposited film. Therefore, the bulk defect density of the CBO absorber film shall influence the overall solar cell performance. [Figure 3.4](#) shows the effect of bulk defect density variation in the CBO light absorber film on solar cell performance comprising various sulfide buffer layers. The increase in the bulk defect density in the CBO layer has reduced the PCE for all distinct n-type MSs buffer layers. Even though PCE values reduced (21.32 to 2.95 %, 22.84 to 5.08 %, and 22.33 to 2.22 % for CdS, WS<sub>2</sub>, and ZnS, respectively) with increased bulk defect density, a lesser reduction is observed for SnS<sub>2</sub> (i.e., 20.9 to 7.56 %). Likewise, a reduction in  $J_{sc}$  and  $V_{oc}$  is observed with an increase in defect density in CBO film, but the FF remained reasonably identical. The reduction in  $J_{sc}$  and  $V_{oc}$  can be attributed to defect-assisted recombination in CBO absorber films and change in band offsets between MS and CBO films resulting from the modification in conduction and valence band levels of CBO films with increased bulk defect density, respectively.[84] The reason behind identical values of FF is not well understood.

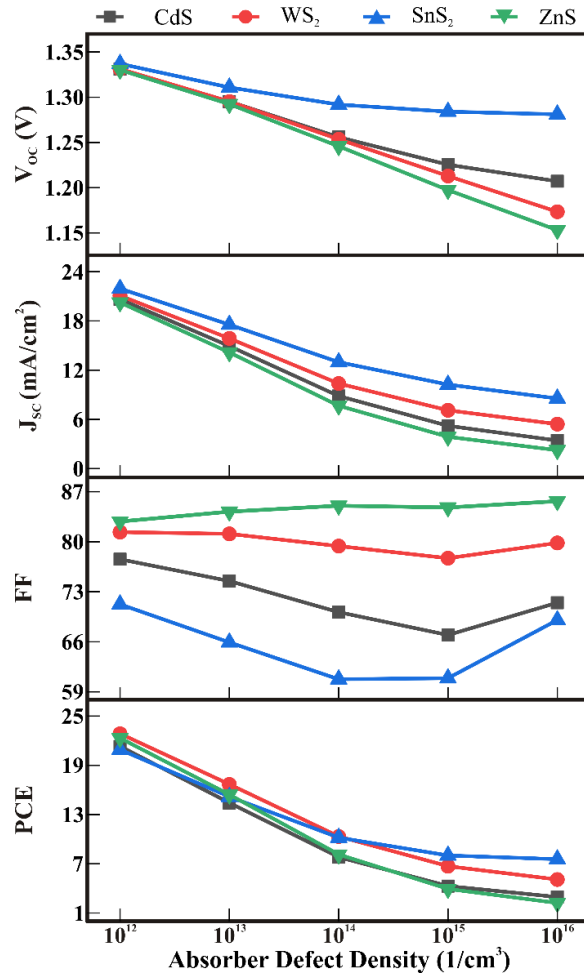


**Figure 3.4** The effect of bulk defect density of 900 nm thick CBO light absorber film on the performance of solar cells comprising various sulfide buffer layers of 100 nm thickness.

### 3.1.5 Donor thickness Optimization

Further, to evaluate the optical and electrical properties of the n-type MSs, the optimized CBO film of 900 nm thickness is considered for the solar cell. [Figure 3.4](#) shows the effect of MS buffer layer thickness on the performance of kusachiite solar cells. The thickness of MS buffer layers is varied independently from 30 to 400 nm to avoid blinding irradiation striking over the CBO absorber films. The PCE and J<sub>sc</sub> marginally increased with increasing thickness of the MS buffer layer for all MSs due to their reasonable visible light photovoltaic activity.[53] However, V<sub>oc</sub> and FF have remained constant as the band offset between the MS and CBO films remain stable irrespective of the increase in the MS film thickness. The V<sub>oc</sub>, and FF depend on the band offset energy level and the internal parasitic resistance, which is independent of the buffer layer thickness.[79]However, considerable

variation in FF for the SnS<sub>2</sub> buffer layer can be assigned to the high intrinsic charge conductivity. Moreover, the PCE of kusachiite solar cells consisting of the SnS<sub>2</sub> buffer layer is relatively higher than that of CdS, ZnS, and WS<sub>2</sub>, which has also linearly enhanced with increased thickness due to its high intrinsic visible photovoltaic activity, which further added up with the CBO absorber layer. However, an increase in metal sulfide buffer layer thickness beyond 400 nm will prevent irradiation from striking the CBO light absorber and insignificantly improve the PCE. Therefore, 100 nm thickness of all buffer layers is considered for further optimizations due to the relatively significant PCE values observed for solar cells consisting of 900 nm CBO absorber layer and 100 nm thick MSs buffer layers. However, for the SnS<sub>2</sub> buffer layer with 400 nm thickness, we were able to achieve maximum efficiency of ~ 30 % at a higher acceptor doping density of 10<sup>22</sup> cm<sup>-3</sup>.

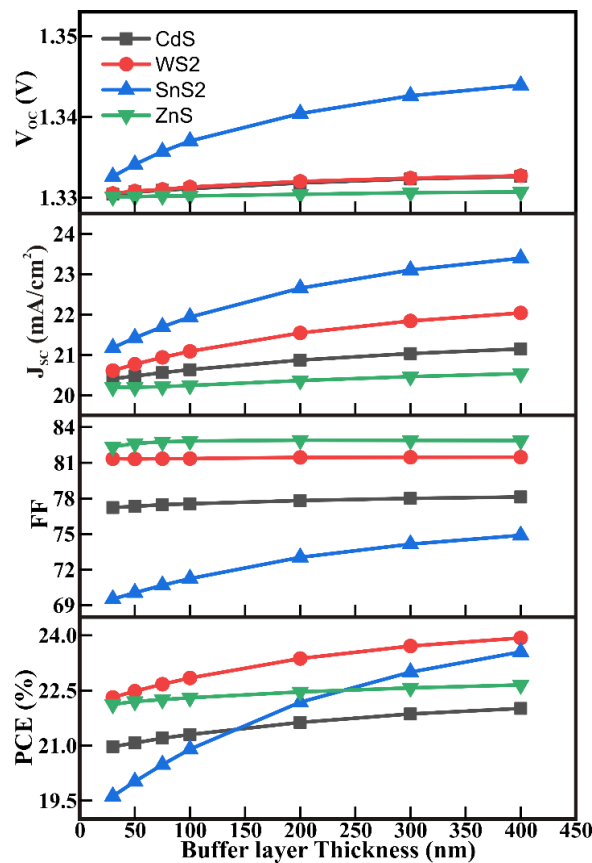


**Figure 3.4** The effect of thickness of MSs buffer layers on the performance of solar cells comprising 900 nm thick CBO absorber layer.

### 3.1.6 Donor density Optimization

Figure 3.5 shows the donor doping density-dependent variation (i.e., 10<sup>15</sup> to 10<sup>22</sup> cm<sup>-3</sup>) in the parameters of CBO/MSs kusachiite solar cells. The increased

donor doping density in the MS films has not significantly altered the PCE,  $V_{oc}$ , FF, and  $J_{sc}$ . Thus, unlike CBO light absorber films, the increase in doping density of MS films had a negligible influence on solar cell performance, and hence, doping of MSs buffer layers has shown not much improvement in increasing the charge conductivity and boost the efficiency of CBO solar cells. Nevertheless, the PCE and  $J_{sc}$  have substantially enhanced with an increase in donor doping density in buffer layers.

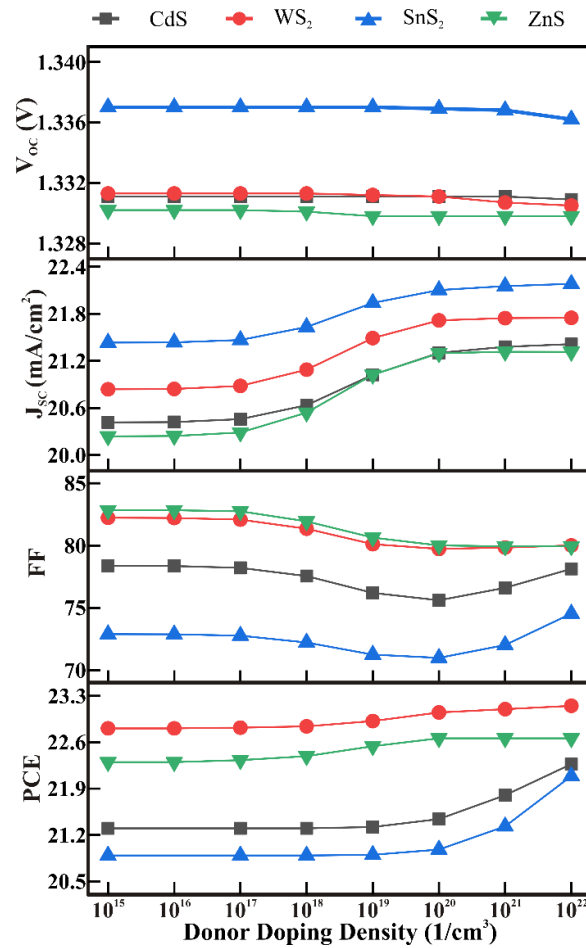


**Figure 3.5** The effect of donor density of 100nm thick MSs buffer layers on the performance of solar cells comprising CBO absorber layer of 900 nm thickness.

### 3.1.7 Work Function Optimization

The metals like Ag, Au, Al, Pt, etc., exhibiting distinct work functions, have been explored as the counter electrode or metal back contacts for the commercial solar cells. Their conductivity, cost, and physical and chemical reactivity directly impact the cost and performance of solar cells. Therefore, the effect of the work function of the metal back contact on the overall performance of solar cells is

explored and shown in Figure 3.6. The work function of electron-rich metal back contact has revealed a direct influence on the performance of solar cells. The  $V_{OC}$  increased sharply up to a work function of 5.1 eV (i.e., Au metal) and saturated thereafter as the holes are easily extracted to metal surfaces with a work function greater than 5.1 eV. The increase in  $J_{SC}$  with work function can be associated with the variable charge extraction due to the difference in the work function of the metal counter electrodes. Moreover, the FF and PCE have significantly increased at work-function of 5.1 eV and thereafter remained relatively perpetual up to 5.7 eV (i.e., Pt metal). The higher PCE and FF values at the work function of 5 eV (i.e., Au metal) indicate the effective hole transfer at the interface of the back metal contacts and CBO absorber layer. Moreover, the  $WS_2$  has delivered a higher PCE of 22.84 % among all other MS buffer layers when combined with the CBO absorber layer and Au metal contact.

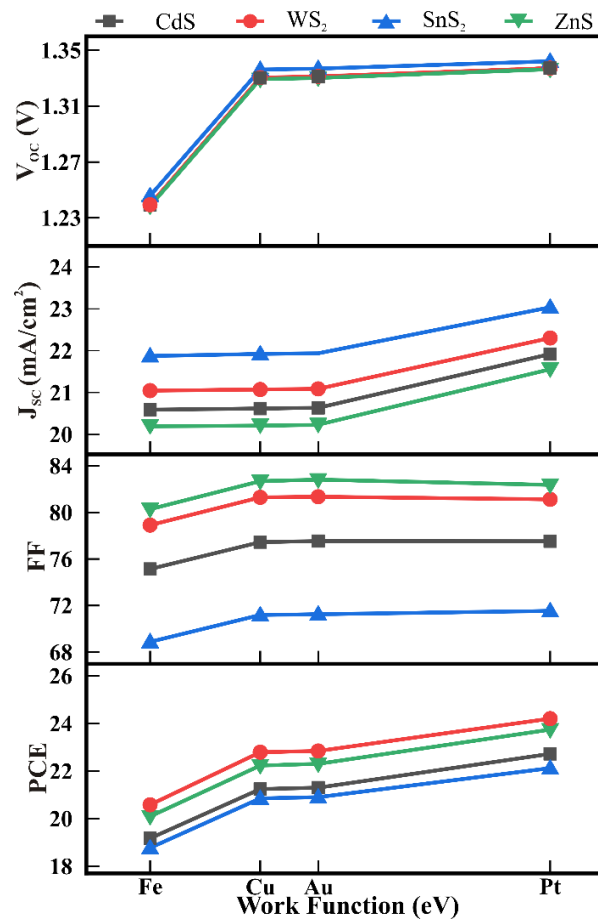


**Figure 3.6** The effect of work-function of metal back contact on various parameters of solar cells consisting of optimized CBO and MSs thin layers.

### 3.1.8 IPCE Variation

Analyzing the spectral response of the CBO and metal sulfide-based kusachiite solar cells is imperative to interpret the overall quantum efficiency. [Figure 3.7](#) shows the incident photon to current efficiency (i.e., IPCE) curves of the kusachiite solar cells made of different thicknesses of CBO absorber film while retaining optimized thickness of 100 nm for CdS, WS<sub>2</sub>, ZnS, and SnS<sub>2</sub> buffer layers. For all the MS films, with increasing thickness of CBO absorber film, the quantum efficiency of solar cells has increased with the CBO absorber thickness generating larger photoelectrons, irrespective of the kind of metal sulfide used as the buffer layer. However, further increase in thickness of CBO (i.e., > 900 nm) restrict the photons from reaching deep inside and progressively generate the photoelectrons, as noticed in CBO absorber thickness-dependent studies ([Figure 3.2](#)). The distinctive bandgap and band-alignment of MSs and CBO have reflected in two distinct dips in IPCE, assigned to the MSs buffer layer and CBO absorber, respectively. The improved IPCE for the SnS<sub>2</sub> buffer layer compared to other MSs reflected through the border curve indicates its better photovoltaic activities with the CBO buffer layer. Moreover, the perfect band alignment of SnS<sub>2</sub> and CBO has shifted this dip to a high wavelength (~ 826 nm), indicating excellent transfer of photogenerated electrons at the interface producing higher IPCE.

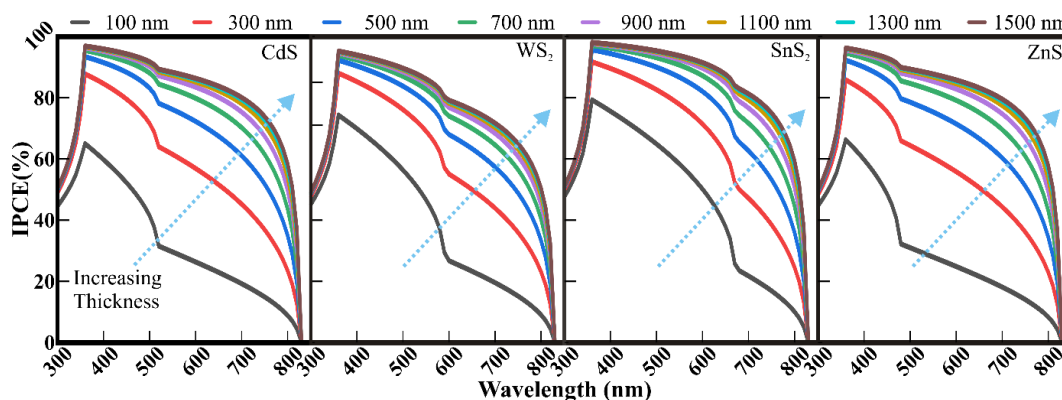


**Figure 3.7** IPCE curves of the kusachiite solar cells for different CBO absorber thicknesses with optimized thickness of various (a) CdS, (b) WS<sub>2</sub>, (c) SnS<sub>2</sub>, and (d) ZnS buffer layers.

### 3.1.9 Optimum efficiency and Temperature Dependence

[Figure 3.8](#) shows the J-V curves of kusachiite solar cells constituted of spinel CBO absorber and distinct n-type buffer layer of CdS, WS<sub>2</sub>, SnS<sub>2</sub>, and ZnS in the dark and under illumination. The kusachiite solar cells consisting of CBO

absorber layer jointly with n-type WS<sub>2</sub> buffer layer delivered higher efficiency of 22.84 %, which is followed by ZnS (21.94 %), CdS (21.3 %), and SnS<sub>2</sub> (20.9 %). However, it is to be noted that a PCE of 23.15 % can be achieved from 100 nm thick n-type WS<sub>2</sub> buffer layer if one can increase the donor doping density up to 10<sup>22</sup> cm<sup>-3</sup> (Figure 8). Higher efficiency, around 27 %, is observed when varied the acceptor doping density. During the real-time application of solar cells, elevated operating temperatures increase stresses associated with thermal expansion and hence play a prominent role in influencing the performance of the cells. Therefore, the effect of the operating temperature is investigated for the temperature ranging from 300 to 380 K, and the corresponding simulated J-V curve is shown in Figure 3.9. The rise in temperature from 300 to 380 K scale down the relative V<sub>OC</sub> by increasing the reverse saturation current, and hence the corresponding PCE decreases. [85] Though the PCE declines with the rise in temperature, reasonable higher efficiency of 21.14 % (at 380 K) is still achieved theoretically for kusachiite solar cells bringing together the 900 nm thick CBO absorber layer and n-type WS<sub>2</sub> buffer layer of 100 nm thickness.

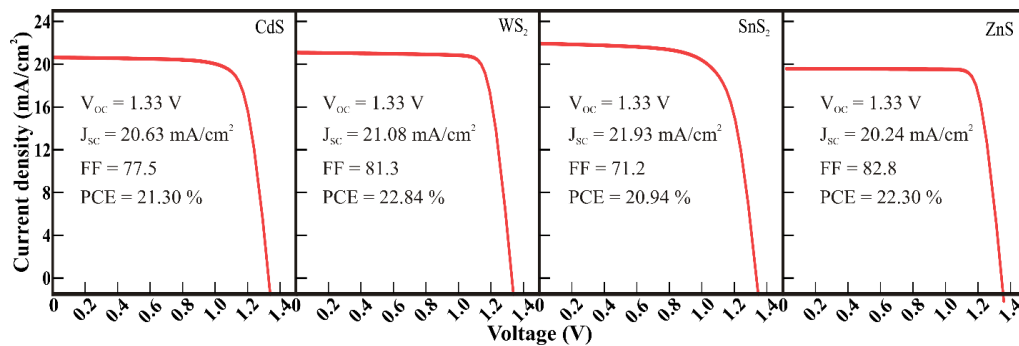


**Figure 3.8** J-V curves of kusachiite solar cells comprising spinel CBO absorber and n-type CdS, WS<sub>2</sub>, SnS<sub>2</sub>, and ZnS buffer layer.

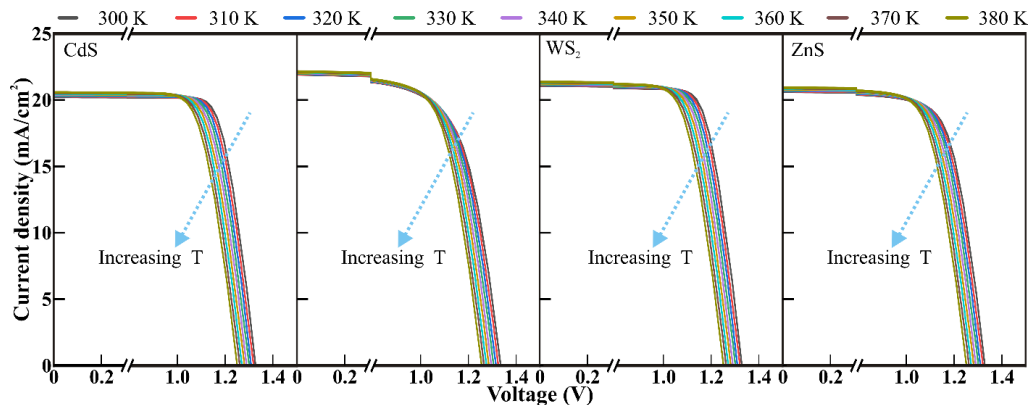


**Figure 3.9** Temperature-dependent J-V curves of the kusachiite solar cells containing spinel CBO absorber and n-type MSs buffer layer.

## 3.2 Experimental Results

### 3.2.1 FESEM Images and EDS Spectroscopy

FESEM analysis was performed using JEOL JSM-6500F to check the morphology of the obtained nanostructure. [Figure 3.10](#) shows the top view FESEM image of the as-synthesized CBO nanostructure. [Figure 3.10 \(a and b\)](#) show the low and high magnification FESEM images of the CBO nanostructure, respectively. Formation of microsphere kind morphology is obtained for CBO nanostructure with a diameter  $\sim 15 \mu\text{m}$ . The micrographs revealed that the CBO microspheres consist of nanorods projecting outside. The size of the nanorods is in the range of 100 nm. These microspheres of hierarchically grown nanorods are highly porous and, therefore, provide a higher surface area for photocatalytic applications.

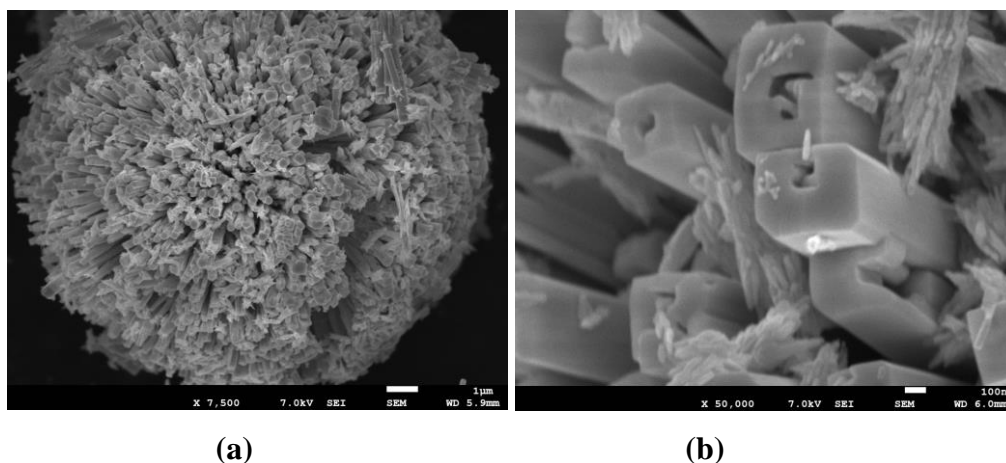


**Figure 3.10** FESEM images of hydrothermally synthesized  $\text{CuBi}_2\text{O}_4$  powder

EDS analysis was performed using Oxford instrument INCA, X-sight 7557, to find the elemental composition of the as-synthesized CBO microsphere. [Figure 3.11](#) shows the EDS spectra of the as-synthesized CBO microsphere. The peaks obtained in EDS spectra at different energy level confirms the presence of Cu, Bi, and O in our material. The absence of unidentified peaks indicating any other material excludes the possibility of any impurity present in our material. Thus, we have synthesized the CBO microsphere without any impurity.

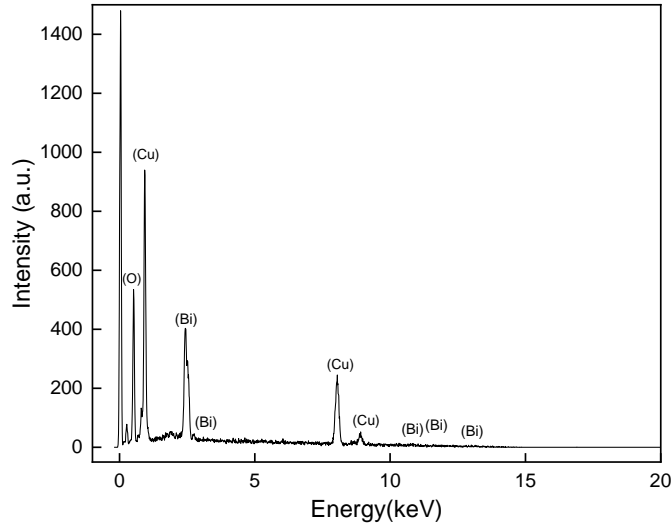


**Figure 3.11** EDS spectrum of hydrothermally synthesized CuBi<sub>2</sub>O<sub>4</sub> powder

### 3.2.2 X-ray Diffraction spectra

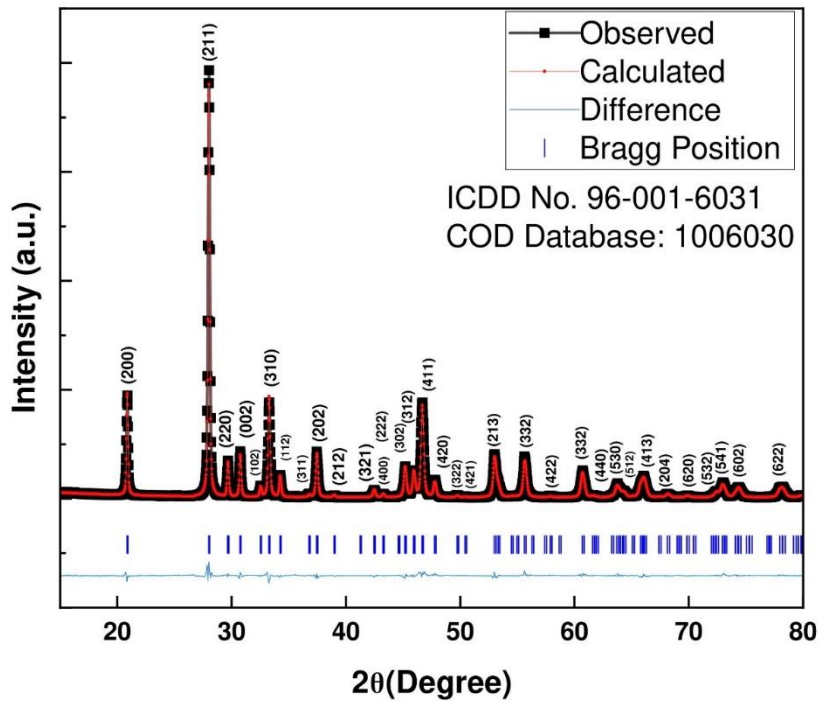


**Figure 3.12** Rietveld Refined Pattern of Pure phase of CBO

X-ray diffraction studies were performed using D2-phase Bruker XRD equipped with a Cu K $\alpha$  radiation ( $\lambda = 1.5405 \text{ \AA}$ ) to confirm the crystal structure and phase purity of the obtained nanostructure. [Figure 3.12](#) shows the Rietveld refined XRD spectra of the as-synthesized CBO nanostructure. XRD spectra confirm the formation of a highly crystalline CBO microsphere with a tetragonal crystal structure. The obtained pattern is well-matched with ICDD reference no. 96-001-

6031. Rietveld analysis of the nanostructure was performed, and the obtained parameters are listed below (Table 3). The refined spectra are well fitted with space group P4/ncc of CBO nanostructure.

Table 3: Parameters obtained from Rietveld Refinement are given below

Goodness of fit	3.19
R-Factors	5.12,6.84
$(R_p)$	7.38
$(R_{wp})$	8.72
$(R_{exp})$	4.88
$a = b$	8.510825
$c$	5.812498
$\alpha = \beta = \gamma$	$90^0$
Chi-squared ( $\chi^2$ )	$\frac{R_{wp}}{R_{exp}} = 1.7868852459$
Bragg Factor ( $R_b$ )	3.15
Structure Factor ( $R_f$ )	2.2

### 3.2.3 UV-Vis Spectroscopy

UV-Visible diffuse reflectance spectroscopy was performed using Shimadzu UV-2600 and shown in [Figure 3.13](#). The corresponding Kubelka-Munk curve was plotted to calculate the bandgap of the CBO nanostructure shown in [Figure 3.14](#). The as-synthesized CBO microsphere is highly photoactive in nature and is confirmed by the obtained bandgap of 1.7 eV, which lies in the visible region.

Kubelka-Munk method was used to determine bandgap through DRS setup by integrated sphere assembly with pure BaSO<sub>4</sub> powder as a reference. The sample is in powder form; the experiment is carried out in reflection mode.

$$F(R) = \frac{(1 - R)^2}{2R}$$

$F(R)$  is the function proposed to estimate bandgap through DRS setup. The numerator in the equation is the absorption co-efficient ( $K$ ), and the denominator is the scattering co-efficient ( $S$ ).

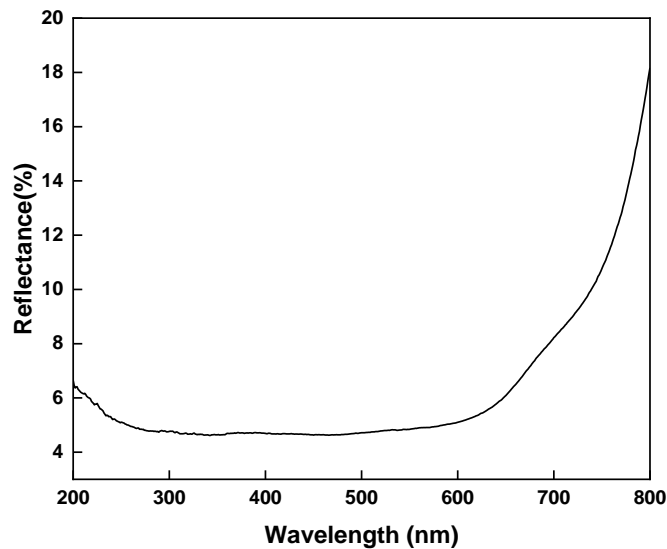


**Figure 3.13** UV-Vis diffuse reflectance spectroscopy of CBO nanostructure

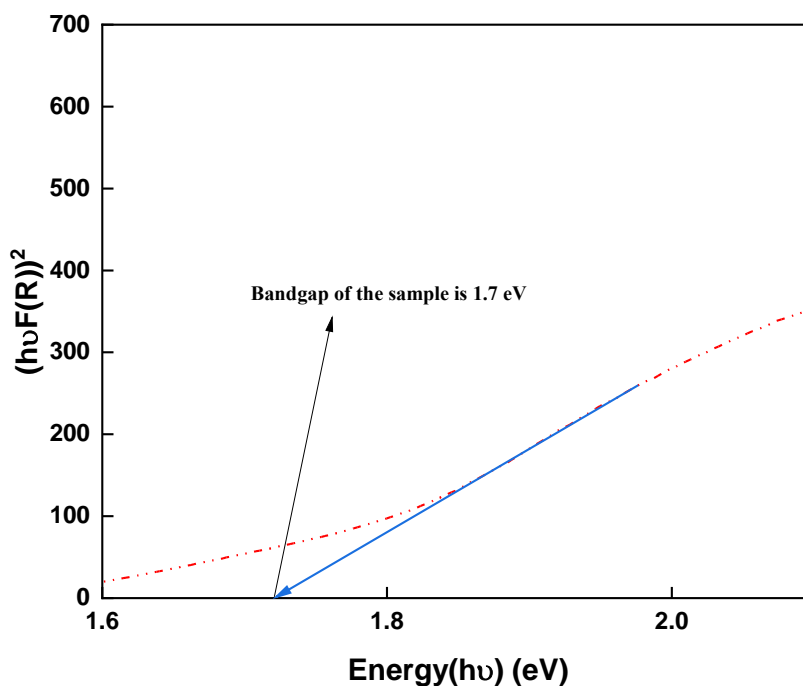


**Figure 3.14** Kubelka-Munk plot of as-synthesized CBO nanostructure

### 3.2.4 X-ray Photoelectron Spectroscopy

XPS (Thermo Scientific Inc. K-alpha) was used to determine the chemical composition and element state of the prepared samples. [Figure 3.15](#) shows core level XPS spectra of Bi, O, and Cu. For Bi, the two peaks observed at a binding

energy of 158.6 eV and 163.9 eV, corresponding to Bi(4f<sub>7/2</sub>) and Bi(4f<sub>5/2</sub>), respectively, indicating the presence of Bi<sup>3+</sup>. For Cu, the peak at a binding energy of 955.5 eV and 935.6 eV, along with the satellite peak at 964.8 eV and 932.8 eV was assigned to Cu(2p<sub>1/2</sub>) and Cu(2p<sub>3/2</sub>), respectively, which confirms that Cu is present in Cu<sup>2+</sup>. [86, 87] For O(1s) spectra, the peak present at the binding energy of 529.4 eV corresponds to the lattice oxygen in the CBO sample.

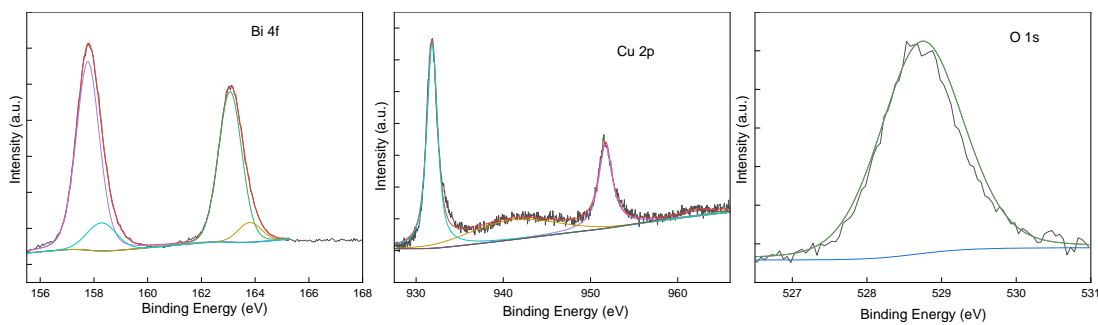


**Figure 3.15** XPS Plots of the powder sample



## Chapter 4

# Conclusions and Future Scope

### 4.1 Conclusions

In conclusion, an oxide spinel CBO and metal sulfide-based kusachiite solar cells are theoretically scrutinized for their best performance as a visible light harvester. Various n-type MS buffer layers (CdS, WS<sub>2</sub>, SnS<sub>2</sub>, and ZnS) are analyzed with p-type kusachiite CBO light absorber to evaluate theoretically (using SCAPS-1D) the performance of CBO based solar cells. All these MSs buffer layers used with CBO have shown efficiencies greater than 20 %. Still, comparatively, the optimized CBO light absorber of the thickness of 900 nm and acceptor doping density of  $2 \times 10^{18} \text{ cm}^{-3}$  with n-type WS<sub>2</sub> buffer layer of 100 nm thickness and  $2 \times 10^{18} \text{ cm}^{-3}$  donor doping density showed the highest PCE of 26.99 %. Therefore, synthesis of CBO light absorber using the cost-effective chemical method and further spin coating or doctor blading it along with the widely employed MSs buffer layer in second and third-generation solar cells, to form kusachiite solar cells, has tremendous potential to gain higher PCE experimentally and compete with perovskite solar cell technology. Overall, the methodology and approach provided here to scrutinize environmentally friendly, cost-effective, easy to manufacture, and packaging visible light absorber and metal sulfide buffer layers can be extended to other optoelectronic devices. Therefore, CBO is synthesized by the hydrothermal method and is subjected to both XRD and spectroscopic measurements. Those experiments revealed that the as-synthesized CBO shows the morphology of rods projecting out from a sphere are of tetragonal phase with space group P4/ncc. The CBO microspheres revealed a bandgap of around 1.7eV. XPS studies confirm the formation of CBO with oxidation states Bi<sup>3+</sup>, Cu<sup>2+</sup> and O<sub>2</sub><sup>-</sup>.

### 4.2 Future scope

The CBO absorber is observed as good absorber with bandgap on 1.7 eV so it shall be explored with metal sulfides and metal oxides for the fabrication of the

solar cell. Such solar cell will have better lifetime and has capability to compete with perovskite solar cells in terms of efficiency.

## References

1. Thomas, N. *Solar's Share in India's Installed Power Capacity Mix Rises to 9.8% as of Q1 2020*. 2020; Available from: <https://mercomindia.com/solar-share-india-installed-power-capacity-mix/>.
2. Smalley, R.E., *Future Global Energy Prosperity: The Terawatt Challenge*. MRS Bulletin, 2005. **30**(6): p. 412-417.
3. Saadatian, O., et al., *Trombe walls: A review of opportunities and challenges in research and development*. Renewable and Sustainable Energy Reviews, 2012. **16**(8): p. 6340-6351.
4. Ibn-Mohammed, T., et al., *Perovskite solar cells: An integrated hybrid lifecycle assessment and review in comparison with other photovoltaic technologies*. Renewable and Sustainable Energy Reviews, 2017. **80**: p. 1321-1344.
5. Müller, G. and J. Friedrich, *Crystal Growth, Bulk: Methods*, in *Encyclopedia of Condensed Matter Physics*, F. Bassani, G.L. Liedl, and P. Wyder, Editors. 2005, Elsevier: Oxford. p. 262-274.
6. Stachurski, Z.H., G. Wang, and X. Tan, *Chapter 2 - Making of metallic glasses and applications*, in *An Introduction to Metallic Glasses and Amorphous Metals*, Z.H. Stachurski, G. Wang, and X. Tan, Editors. 2021, Elsevier. p. 9-44.
7. Ramanujam, J., et al., *Flexible CIGS, CdTe and a-Si:H based thin film solar cells: A review*. Progress in Materials Science, 2020. **110**: p. 100619.
8. Lee, T.D. and A.U. Ebong, *A review of thin film solar cell technologies and challenges*. Renewable and Sustainable Energy Reviews, 2017. **70**: p. 1286-1297.
9. Yan, J. and B.R. Saunders, *Third-generation solar cells: a review and comparison of polymer:fullerene, hybrid polymer and perovskite solar cells*. RSC Advances, 2014. **4**(82): p. 43286-43314.
10. Ji, G., et al., *12.88% efficiency in doctor-blade coated organic solar cells through optimizing the surface morphology of a ZnO cathode buffer layer*. Journal of Materials Chemistry A, 2019. **7**(1): p. 212-220.
11. Ameri, T., et al., *Organic tandem solar cells: A review*. Energy & Environmental Science, 2009. **2**(4): p. 347-363.

12. Romeo, A. and E. Artegiani, *CdTe-Based Thin Film Solar Cells: Past, Present and Future*. *Energies*, 2021. **14**(6).
13. Bisquert, J. and E.J. Juarez-Perez, *The Causes of Degradation of Perovskite Solar Cells*. *The Journal of Physical Chemistry Letters*, 2019. **10**(19): p. 5889-5891.
14. Lohrasbi, M., et al. *Degradation study of dye-sensitized solar cells by electrochemical impedance and FTIR spectroscopy*. in *2013 IEEE Energytech*. 2013.
15. Greijer Agrell, H., J. Lindgren, and A. Hagfeldt, *Degradation mechanisms in a dye-sensitized solar cell studied by UV–VIS and IR spectroscopy*. *Solar Energy*, 2003. **75**(2): p. 169-180.
16. Lu, H.-L., et al., *The degradation of dye sensitized solar cell in the presence of water isotopes*. *Solar Energy Materials and Solar Cells*, 2011. **95**(7): p. 1624-1629.
17. Znajdek, K., et al., *Polymer substrates for flexible photovoltaic cells application in personal electronic system*. *Opto-Electronics Review*, 2016. **24**(1): p. 20-24.
18. Kim, J., K.S. Kim, and C.W. Myung, *Efficient electron extraction of SnO<sub>2</sub> electron transport layer for lead halide perovskite solar cell*. *npj Computational Materials*, 2020. **6**(1): p. 100.
19. Zheng, S., et al., *Materials and structures for the electron transport layer of efficient and stable perovskite solar cells*. *Science China Chemistry*, 2019. **62**(7): p. 800-809.
20. Bag, A., et al., *Effect of absorber layer, hole transport layer thicknesses, and its doping density on the performance of perovskite solar cells by device simulation*. *Solar Energy*, 2020. **196**: p. 177-182.
21. Nande, A., S. Raut, and S.J. Dhoble, *Chapter 9 - Perovskite solar cells*, in *Energy Materials*, S.J. Dhoble, et al., Editors. 2021, Elsevier. p. 249-281.
22. Tsurkan, V., et al., *On the complexity of spinels: Magnetic, electronic, and polar ground states*. *Physics Reports*, 2021. **926**: p. 1-86.
23. Biagioni, C. and M. Pasero, *The systematics of the spinel-type minerals: An overview*. *American Mineralogist*, 2014. **99**(7): p. 1254-1264.

24. Ali, J., et al., *Elucidating the Roles of Hole Transport Layers in p-i-n Perovskite Solar Cells*. *Advanced Electronic Materials*, 2020. **6**(12): p. 2000149.
25. Hussain, I., et al., *Functional materials, device architecture, and flexibility of perovskite solar cell*. *Emergent Materials*, 2018. **1**(3): p. 133-154.
26. "Honsberg, C.B. and S.G. "Bowden. *Photovoltaics Education Website*. 2019; Available from: <https://www.pveducation.org/>.
27. Hubbard, S., *Recombination*. *Photovoltaic Solar Energy*, 2016: p. 39-46.
28. Shanmugam, N., et al., *Anti-Reflective Coating Materials: A Holistic Review from PV Perspective*. *Energies*, 2020. **13**(10).
29. Kim, M.S., J.H. Lee, and M.K. Kwak, *Review: Surface Texturing Methods for Solar Cell Efficiency Enhancement*. *International Journal of Precision Engineering and Manufacturing*, 2020. **21**(7): p. 1389-1398.
30. Sprafke, A.N. and R.B. Wehrspohn, *Current Concepts for Optical Path Enhancement in Solar Cells*. *Photon Management in Solar Cells*, 2015: p. 1-20.
31. Würfel, P., *Basic Structure of Solar Cells*. *Physics of Solar Cells*, 2005: p. 109-136.
32. Swatowska, B., et al., *The Role of Antireflection Coatings in Silicon Solar Cells – The Influence on Their Electrical Parameters*. *Optica Applicata*, 2011. **XLI**: p. 487.
33. Debije, M.G. and P.P.C. Verbunt, *Thirty Years of Luminescent Solar Concentrator Research: Solar Energy for the Built Environment*. *Advanced Energy Materials*, 2012. **2**(1): p. 12-35.
34. Al-Shahri, O.A., et al., *Solar photovoltaic energy optimization methods, challenges and issues: A comprehensive review*. *Journal of Cleaner Production*, 2021. **284**: p. 125465.
35. Green, M.A., *How Did Solar Cells Get So Cheap?* *Joule*, 2019. **3**(3): p. 631-633.
36. He, M., et al., *Kesterite Solar Cells: Insights into Current Strategies and Challenges*. *Advanced Science*, 2021. **8**(9): p. 2004313.
37. Kurley, J.M., et al., *Roll-To-Roll Friendly Solution-Processing of Ultrathin, Sintered CdTe Nanocrystal Photovoltaics*. *ACS Applied Materials & Interfaces*, 2021. **13**(37): p. 44165-44173.

38. Wei, Z., et al., *Successes and Challenges Associated with Solution Processing of Kesterite Cu<sub>2</sub>ZnSnS<sub>4</sub> Solar Cells on Titanium Substrates*. ACS Applied Energy Materials, 2020. **3**(4): p. 3876-3883.
39. Kim, T.S., et al., *Ultra-Lightweight, Flexible InGaP/GaAs Tandem Solar Cells with a Dual-Function Encapsulation Layer*. ACS Applied Materials & Interfaces, 2021. **13**(11): p. 13248-13253.
40. Karthikeyan, V., et al., *Hydrothermally tailored anatase TiO<sub>2</sub> nanoplates with exposed {111} facets for highly efficient dye-sensitized solar cells*. Solar Energy, 2017. **147**: p. 202-208.
41. Manjunath, V., et al., *Oxidized Nickel films as highly transparent HTLs for inverted planar perovskite solar cells*. Solar Energy, 2019. **193**: p. 387-394.
42. Maniarasu, S., et al., *Recent advancement in metal cathode and hole-conductor-free perovskite solar cells for low-cost and high stability: A route towards commercialization*. Renewable and Sustainable Energy Reviews, 2018. **82**: p. 845-857.
43. Kim, G., et al., *Impact of strain relaxation on performance of formamidinium lead iodide perovskite solar cells*. Science, 2020. **370**(6512): p. 108-112.
44. Aftab, A. and M.I. Ahmad, *A review of stability and progress in tin halide perovskite solar cell*. Solar Energy, 2021. **216**: p. 26-47.
45. Manjunath, V., et al., *Perovskite-Based Facile NiO/CH<sub>3</sub>NH<sub>3</sub>PbI<sub>3</sub> Heterojunction Self-Powered Broadband Photodetector*. ACS Applied Electronic Materials, 2021. **3**(10): p. 4548-4557.
46. Gao, X.-X., et al., *High-Mobility Hydrophobic Conjugated Polymer as Effective Interlayer for Air-Stable Efficient Perovskite Solar Cells*. Solar RRL, 2019. **3**(1): p. 1800232.
47. Ge, C., et al., *Mixed Dimensional Perovskites Heterostructure for Highly Efficient and Stable Perovskite Solar Cells*. Solar RRL. **n/a**(n/a): p. 2100879.
48. Li, J., et al., *Suppressing Interfacial Shunt Loss via Functional Polymer for Performance Improvement of Lead-Free Cs<sub>2</sub>AgBiBr<sub>6</sub> Double Perovskite Solar Cells*. Solar RRL. **n/a**(n/a): p. 2100791.

49. Du, Y., et al., *Ionic Liquid Treatment for Highest-Efficiency Ambient Printed Stable All-Inorganic CsPbI<sub>3</sub> Perovskite Solar Cells*. *Advanced Materials*. **n/a**(n/a): p. 2106750.
50. Liu, S., et al., *Pulsed laser/ electrodeposited CuBi<sub>2</sub>O<sub>4</sub>/BiVO<sub>4</sub> p-n heterojunction for solar water splitting*. *Solar Energy Materials and Solar Cells*, 2018. **180**: p. 123-129.
51. Sabri, M., A. Habibi-Yangjeh, and S. Ghosh, *Novel ZnO/CuBi<sub>2</sub>O<sub>4</sub> heterostructures for persulfate-assisted photocatalytic degradation of dye contaminants under visible light*. *Journal of Photochemistry and Photobiology A: Chemistry*, 2020. **391**: p. 112397.
52. Zhu, L., et al., *Visible Light-Induced Photoelectrochemical and Antimicrobial Properties of Hierarchical CuBi<sub>2</sub>O<sub>4</sub> by Facile Hydrothermal Synthesis*. *ChemistrySelect*, 2016. **1**(8): p. 1518-1524.
53. He, Z., et al., *Recent progress in metal sulfide-based electron transport layers in perovskite solar cells*. *Nanoscale*, 2021. **13**(41): p. 17272-17289.
54. Moon, D.G., et al., *A review on binary metal sulfide heterojunction solar cells*. *Solar Energy Materials and Solar Cells*, 2019. **200**: p. 109963.
55. Ouyang, Y., et al., *Photo-oxidative degradation of methylammonium lead iodide perovskite: mechanism and protection*. *Journal of Materials Chemistry A*, 2019. **7**(5): p. 2275-2282.
56. Hosen, A., M.S. Mian, and S.R.A. Ahmed, *Simulating the performance of a highly efficient CuBi<sub>2</sub>O<sub>4</sub>-based thin-film solar cell*. *SN Applied Sciences*, 2021. **3**(5): p. 544.
57. Alla, M., et al., *Optimized CH<sub>3</sub>NH<sub>3</sub>PbI<sub>3</sub>-XCIX based perovskite solar cell with theoretical efficiency exceeding 30%*. *Optical Materials*, 2022. **124**: p. 112044.
58. Karthick, S., S. Velumani, and J. Bouclé, *Experimental and SCAPS simulated formamidinium perovskite solar cells: A comparison of device performance*. *Solar Energy*, 2020. **205**: p. 349-357.
59. Zhou, Z., et al., *Interface engineering for high-performance perovskite hybrid solar cells*. *Journal of Materials Chemistry A*, 2015. **3**(38): p. 19205-19217.

60. Rai, N., et al., *Analysis of various ETL materials for an efficient perovskite solar cell by numerical simulation*. Journal of Materials Science: Materials in Electronics, 2020. **31**(19): p. 16269-16280.
61. Salah, M.M., et al., *A comparative study of different ETMs in perovskite solar cell with inorganic copper iodide as HTM*. Optik, 2019. **178**: p. 958-963.
62. Samiee, M., et al., *Defect density and dielectric constant in perovskite solar cells*. Applied Physics Letters, 2014. **105**(15): p. 153502.
63. Hosen, M.B., et al., *Performance Optimization of ZnS/CIGS Solar Cell With Over 25% Efficiency Enabled by Using a CuIn<sub>3</sub>Se<sub>5</sub> OVC Layer*. INTERNATIONAL JOURNAL OF RENEWABLE ENERGY RESEARCH, 2020. **10**(4): p. 2000-2005.
64. Tripathi, S., B. Kumar, and D.K. Dwivedi, *Numerical simulation of non-toxic In<sub>2</sub>S<sub>3</sub>/SnS<sub>2</sub> buffer layer to enhance CZTS solar cells efficiency by optimizing device parameters*. Optik, 2021. **227**: p. 166087.
65. Haghghi, M., et al., *A modeling study on utilizing SnS<sub>2</sub> as the buffer layer of CZT(S, Se) solar cells*. Solar Energy, 2018. **167**: p. 165-171.
66. Sobayel, K., et al., *Efficiency enhancement of CIGS solar cell by WS<sub>2</sub> as window layer through numerical modelling tool*. Solar Energy, 2020. **207**: p. 479-485.
67. Islam, A.M., et al., *Performance analysis of tungsten disulfide (WS<sub>2</sub>) as an alternative buffer layer for CdTe solar cell through numerical modeling*. Optical Materials, 2021. **120**: p. 111296.
68. Sharma, S., et al., *Nanostructured Materials for Food Applications: Spectroscopy, Microscopy and Physical Properties*. Bioengineering, 2019. **6**(1).
69. Epp, J., *4 - X-ray diffraction (XRD) techniques for materials characterization*, in *Materials Characterization Using Nondestructive Evaluation (NDE) Methods*, G. Hübschen, et al., Editors. 2016, Woodhead Publishing. p. 81-124.
70. Rocha, F.S., et al., *Experimental methods in chemical engineering: Ultraviolet visible spectroscopy—UV-Vis*. The Canadian Journal of Chemical Engineering, 2018. **96**(12): p. 2512-2517.

71. Bajpai, P., *Chapter 11 - Optical Properties of Paper*, in *Biermann's Handbook of Pulp and Paper (Third Edition)*, P. Bajpai, Editor. 2018, Elsevier. p. 237-271.
72. Roy, A., R. Ramasubramaniam, and H. Gaonkar, *Empirical relationship between Kubelka-Munk and radiative transfer coefficients for extracting optical parameters of tissues in diffusive and nondiffusive regimes*. *Journal of biomedical optics*, 2012. **17**: p. 115006.
73. De Wolf, S., et al., *Organometallic Halide Perovskites: Sharp Optical Absorption Edge and Its Relation to Photovoltaic Performance*. *The Journal of Physical Chemistry Letters*, 2014. **5**(6): p. 1035-1039.
74. Zhao, Y., A.M. Nardes, and K. Zhu, *Solid-State Mesostructured Perovskite CH<sub>3</sub>NH<sub>3</sub>PbI<sub>3</sub> Solar Cells: Charge Transport, Recombination, and Diffusion Length*. *The Journal of Physical Chemistry Letters*, 2014. **5**(3): p. 490-494.
75. Xing, G., et al., *Long-Range Balanced Electron- and Hole-Transport Lengths in Organic-Inorganic CH<sub>3</sub>NH<sub>3</sub>PbI<sub>3</sub>*. *Science*, 2013. **342**(6156): p. 344-347.
76. Wang, F., et al., *Gradient Self-Doped CuBi<sub>2</sub>O<sub>4</sub> with Highly Improved Charge Separation Efficiency*. *Journal of the American Chemical Society*, 2017. **139**(42): p. 15094-15103.
77. Berglund, S.P., et al., *Comprehensive Evaluation of CuBi<sub>2</sub>O<sub>4</sub> as a Photocathode Material for Photoelectrochemical Water Splitting*. *Chemistry of Materials*, 2016. **28**(12): p. 4231-4242.
78. Ghosh, H., et al., *Light-Harvesting Properties of Embedded Tin Oxide Nanoparticles for Partial Rear Contact Silicon Solar Cells*. *Plasmonics*, 2017. **12**(6): p. 1761-1772.
79. Liu, Y., et al., *Efficiency of MAPbI<sub>3</sub>-Based Planar Solar Cell Analyzed by Its Thickness-Dependent Exciton Formation, Morphology, and Crystallinity*. *ACS Applied Materials & Interfaces*, 2019. **11**(16): p. 14810-14820.
80. Balach, J., et al., *Metal-based nanostructured materials for advanced lithium–sulfur batteries*. *Journal of Materials Chemistry A*, 2018. **6**(46): p. 23127-23168.

81. Vishwakarma, R., *Effect of substrate temperature on ZnS films prepared by thermal evaporation technique*. Journal of Theoretical and Applied Physics, 2015. **9**(3): p. 185-192.
82. Jassim, S.A.-J., A.A.R.A. Zumaila, and G.A.A. Al Waly, *Influence of substrate temperature on the structural, optical and electrical properties of CdS thin films deposited by thermal evaporation*. Results in Physics, 2013. **3**: p. 173-178.
83. Rai, S., B.K. Pandey, and D.K. Dwivedi, *Designing hole conductor free tin-lead halide based all-perovskite heterojunction solar cell by numerical simulation*. Journal of Physics and Chemistry of Solids, 2021. **156**: p. 110168.
84. Moon, M.M.A., et al., *Design and Simulation of FeSi<sub>2</sub>-Based Novel Heterojunction Solar Cells for Harnessing Visible and Near-Infrared Light*. physica status solidi (a), 2020. **217**(6): p. 1900921.
85. Sheikh, A.D., et al., *Effects of High Temperature and Thermal Cycling on the Performance of Perovskite Solar Cells: Acceleration of Charge Recombination and Deterioration of Charge Extraction*. ACS Applied Materials & Interfaces, 2017. **9**(40): p. 35018-35029.
86. Brezesinski, K., et al., *Exceptional Photocatalytic Activity of Ordered Mesoporous  $\beta$ -Bi<sub>2</sub>O<sub>3</sub> Thin Films and Electrospun Nanofiber Mats*. Chemistry of Materials, 2010. **22**(10): p. 3079-3085.
87. Zhang, L., et al., *Cu-doped Bi<sub>2</sub>O<sub>3</sub>/Bi<sub>0</sub> composite as an efficient Fenton-like catalyst for degradation of 2-chlorophenol*. Separation and Purification Technology, 2016. **157**: p. 203-208.